Correspondence to:

J.-S. von Storch,
jin-song.von.storch@mpimet.mpg.de

Wind Power Input to Ocean Near-Inertial Waves Diagnosed From a 5-km Global Coupled Atmosphere-Ocean General Circulation Model

Jin-Song von Storch[1,2] and **Veit Lüschow[1]**

[1]Max Planck Institute for Meteorology, Hamburg, Germany, [2]Center for Earth System Research and Sustainability (CEN), Universität Hamburg, Hamburg, Germany

Abstract Using the 5 km coupled general circulation model ICON, the surface internal wave energy source, crucial for the oceanic circulation, is quantified as the wind-induced wave energy flux that radiates from the mixed layer bottom (MLB) into the ocean interior. Our result lowers the previous estimates of the wind power input to surface near-inertial motions from up to more than 1 TW down to about 0.23–0.27 TW, depending on season. We point out that the estimate of the wind input to ocean depends not only on the wind stress used—as suggested by previous studies—but also on the ocean model used. While the surface currents in a slab ocean model or a non-eddying ocean circulation model are strongly determined by the wind forcing, the surface currents in the 5 km ICON model can be more strongly determined by internal instability process (eddy) than by wind stress forcing from less-extreme weather disturbances. The resulting more or less random alignment of surface current and wind stress can presumably lead to a lower wind input to surface near-inertial motions. Of the surface wave energy source, about 30% is fluxed down into the interior ocean. This percentage roughly doubles those from previous studies, due to the stronger wave energy flux related to stronger inertial waves generated by the tropical cyclones simulated by the 5 km ICON model. Overall, the low wind input at near-inertial frequencies produces a wind-induced wave energy source at the MLB that is well below 0.1 TW.

Plain Language Summary For maintaining the oceanic overturning circulation, energy is needed to mix the dense water up and light water down. The main energy source for mixing arises from breaking of internal waves. A considerable portion of this source comes from waves excited by winds at the sea surface. This paper quantifies this wave energy source based on a frontier simulation of a coupled atmosphere-ocean general circulation model at a horizontal resolution of 5 km. This model is capable to simulate tropical cyclones (hurricanes and typhoons) and less-extreme small-scale and short-living weather disturbances and oceanic mesoscale eddies, which were not represented by the models used in most of the previous studies. Taking these new features into account, we find that the wind-induced wave energy source is less than 0.1 TW.

1. Introduction

Together with internal tides and lee waves, near-inertial waves (NIWs) are considered as a main source of the canonical 2 TW of mixing energy required to sustain the global overturning circulation (Ferrari & Wunsch, 2009; Munk & Wunsch, 1998; Wunsch & Ferrari, 2004). Investigating the wind power input to surface near-inertial motions is an important step toward quantifying the power available for interior mixing arising from wind-induced NIWs. This investigation has a long history, beginning with estimates based on the mixed layer slab model of Pollard and Millard (1970) that is forced with observed surface wind stress (Alford, 2001, 2003a; D'asaro, 1985; Jiang et al., 2005; Watanabe & Hibiya, 2002), and followed by estimates based on ocean general circulation models (O-GCMs) that are forced with wind stress from reanalysis products (Flexas et al., 2019; Furuichi et al., 2008; Raja et al., 2022; Rimac et al., 2013). The early studies (mostly based on a slab ocean model) suggest a total wind-induced power input to near-inertial motions around 0.5 TW, whereas the recent studies using O-GCMs at a resolution of about a few kilometers suggest an input around 0.2 TW or below. It was found that the wind power input is sensitive to the spatial and temporal scales of wind stress forcing and can be as large as 1.1–1.4 TW when increasing the resolution of the wind stress forcing (Jiang et al., 2005; Rimac et al., 2013). Here we focus on two aspects that could not have been fully addressed so far and provide a further estimate using a 5-km coupled atmosphere and ocean GCM.

The first aspect concerns tropical cyclones (TC, i.e., hurricanes and typhoons). Tropical cyclones were considered as an important energy provider for diapycnal mixing (Emanuel, 2001). By introducing transient intense diapycnal mixing arising from tropical cyclones into an ocean GCM, Boos et al. (2004) investigated the role of abyssal mixing induced by tropical cyclones for the meridional overturning circulation. Apart from quantifying the effect of TC-induced mixing, there are also quite some studies on the role of tropical cyclones as an efficient generator of NIWs in the ocean. Studies were carried out both from a theoretical point of view, for example, by addressing the ocean's baroclinic response to a rapidly moving storm using an idealized numerical model (Price, 1983), and from observational point of view by analyzing individual tropical cyclones (Firing et al., 1997; Sanford et al., 2011; Yang & Hou, 2014). Liu et al. (2008) went beyond the consideration of individual storms and estimated the mechanical energy input to the world's ocean induced by 1,500 tropical cyclones observed during 1984–2003. The estimate is based on a limited-area coupled model constructed from an axis-symmetric hurricane model and a three-layer ocean model. The result suggests an annual mean TC-induced energy input to near-inertial motions of about 0.03 TW, which is almost 20% of 0.16 TW (Flexas et al., 2019), the lower bound of the range of the previous estimates of total wind-induced power input to near-inertial motions. Another estimate of 0.05 TW was suggested by K. Emanuel according to a review by Alford et al. (2016). It remains unclear whether the role of tropical cyclones as an efficient wave generator of near-inertial motions can be confirmed by a km-scale coupled atmosphere-ocean GCM, and if so, how do the hurricanes alter the strength and spatial distribution of the wind-power input to NIWs in the ocean interior.

The second aspect which has not been examined fully is the energy flux related to NIWs that radiate from the mixed layer bottom (MLB) into the stratified ocean below. This energy flux may be considered as the fraction of the wind power input at the sea surface that "survives" the strong dissipation processes within the mixed layer and becomes available for the interior mixing. Some attempts at estimating this fraction have been made (Alford, 2020; Furuichi et al., 2008; Raja et al., 2022). Theoretical considerations by Gill (1984) and Olbers et al. (2020) relate the NIW energy flux at MLB to internal waves excited by a vertical velocity at MLB that results from divergent mixed layer currents induced by wind stress. Olbers et al. (2020) studied this energy flux by introducing the physics of wave radiation into the slab model of Pollard and Millard (1970). So far the few existing estimates of NIW energy flux at MLB stem from uncoupled ocean GCMs. They suffer from either a too coarse wind forcing frequency and an unrealistic application of surface wind stresses by assuming an ocean at rest or from ignoring the contribution of tropical cyclones. It is hence worthwhile to re-examine this flux using a coupled atmosphere-ocean GCM that represent both the wind stress and the turbulent mixing in a more realistic manner, and is capable to simulate tropical cyclones.

We address both aspects using a frontier simulation performed with the coupled ICON model having a 5 km resolution in both the atmosphere and the ocean. The coupled ICON model has a non-hydrostatic atmospheric component that permits resolving tropical deep convection, one of the major modes of atmospheric heat transports (Stevens et al., 2019). The simulation emerges from the DYMOND (DYnamics of the Atmospheric general circulation Modeled On Non-hydrostatic Domains) project (See https://www.esiwace.eu/services/dyamond-initiative/dyamond-specific-pages-and-material/dyamond-protocol), which is a framework for the intercomparison of an emerging class of atmospheric circulation models. Through their resolution (≤5 km) of the major modes of atmospheric heat transport, DYMOND endeavors to represent the most important scales of the full three-dimensional fluid dynamics of the atmospheric circulation. The project consists of two phases. The first one consists of atmosphere-only simulations over a boreal summer period of 40 days and the second phase consists of both atmosphere-only and coupled atmosphere-ocean simulations over a boreal winter period of 40 days. The coupled 5 km ICON simulation considered in this paper is a product of the second phase of the DYMOND project.

Section 2 provides further details of the 5 km coupled simulation and describes the analysis methods. The wind-induced power to near-inertial motions through the sea surface, that includes the contributions from tropical cyclones, and the NIW energy flux at MLB are diagnosed from this simulation. The result is represented in Section 3, followed by discussions in Section 4. Conclusions are given in Section 5.

2. The ICON Simulation and the Analysis Methods

2.1. The 5-km ICON Simulation

The atmospheric component of the ICON model, the atmospheric ICOsahedral Non-hydrostatic model (ICON-A) (Giorgetta et al., 2018; Zängl et al., 2015), is close to the version used in Hohenegger et al. (2019). The physical parameterizations of deep convection, subgrid-scale orographic effects (blocking and gravity wave drag), and non-orographic gravity wave drag are deactivated. Parameterizations included are the radiative transfer model following Pincus and Stevens (2013) and Pincus et al. (2019), the 3D Smagorinsky turbulent scheme following Dipankar et al. (2015), and a bulk microphysics scheme following Baldauf et al. (2011). The physical properties of the land surface and land-atmosphere fluxes of heat and water are simulated by JSBACH land surface model version 4, a "lite" configuration that includes only the essential physical processes ported from JSBACH v3 (Raddatz et al., 2007). The oceanic component of the ICON model, the ICON-O (Korn, 2017), is close to the version discussed in Korn et al. (2022). The parameterizations of eddy induced diffusion and eddy induced advection are deactivated. The turbulent vertical mixing is parameterized following Gaspar et al. (1990). ICON-O incorporates a sea ice model consisting of dynamic and thermodynamic component. The simulation is run without ocean tides. ICON-A and ICON-O are coupled by exchanging the air-sea fluxes every 15 min. The horizontal resolution is 5 km in both ICON-A and ICON-O, where the grid resolution is defined as the square root of the cell area of the spherical triangles (Zängl et al., 2015). A coarse-resolution variant of the ICON-ESM is described by Jungclaus et al. (2021). Further information on the 5 km coupled ICON simulation can be found in Hohenegger and et al. (2023), Gutjahr et al. (2022) and Mauritsen et al. (2022). A detailed analysis of a tropical cyclone simulated by the 5 km ICON model is carried out by Kumar et al. (2021).

Gutjahr et al. (2022) argued that two features of the ICON model, namely the non-hydrostatic dynamical core and the 5 km horizontal resolution, are essential for representing katabatic storms and the related air-sea interactions impacting on water mass formation in the polar region. We expect that the same two features are also important for representing the wind power input to near-inertial motions in general, and for representing tropical cyclones and their interactions with the underlying ocean in particular. Apart from these features, there are two further ingredients that are important for addressing the two aspects pointed out in Section 1. The first one is the physical parameterization of the wind stress at the sea surface. ICON-A and ICON-O are coupled via an interactive surface flux scheme that determines the surface wind stress based on the relative velocity between the air and the water. This differs from the wind stress calculation transitionally used in the ocean-only simulations at the Max-Planck Institute that assumes an ocean at rest.

The second ingredient is the high vertical resolution, especially in the upper ocean. The ICON-A has 90 terrain-following hybrid sigma levels. The ICON-O has total 128 vertical levels in z-coordinates. The thickness of the first level is 7 m, which is needed to incorporate sea ice and spatial variations in sea level height. The thickness of the second layer is 2 m. Below the second layer and down to 138 m, there are total 43 layers with a thickness of 3 m. This high vertical resolution ensures a more detailed description of processes within the upper ocean, and with that a more realistic representation of the NIW energy flux at the MLB.

The 5 km ICON model was initialized from a coupled state consistent with that of January 20, 2020, and integrated over 21 months. For the initialization of the atmosphere, the 9 km European Center for Medium Range Weather Forecasts (ECMWF) Integrated Forecasting System (IFS) analysis corresponding to January 20, 2020 was used. For the initialization of the ocean, which needs to be spun up first, the ICON-O in a coarser resolution of 10 km was forced by a combination of several atmospheric forcings for over 80 years, with the last 11 years being forced by the ERA5 reanalysis for the period from 2000 to 2010. The ocean state was then interpolated from the 10 km to the 5 km grid and integrated from 2011 to January 2020 using the hourly ERA5 reanalysis (Hersbach et al., 2020) (see also Gutjahr et al. (2022)).

Crucial for the present study is the quality of the wind stress simulated by the coupled ICON model. A one-to-one correspondence between ERA5 reanalysis and ICON simulation cannot be expected mainly due to the chaotic nature of the atmosphere and the short time period considered here. Nevertheless the wind stress simulated by the 5 km ICON model is very comparable to that found in ERA5, both with respect to the mean (not shown) and to the variability (Figure 1). Also well simulated is the seasonal signal, for example, larger seasonal contrast in mean zonal wind stress in Northern Hemisphere than in Southern Hemisphere (not shown) and stronger zonal wind stress variability in the winter hemisphere than in the summer hemisphere (Figure 1). The filaments of large
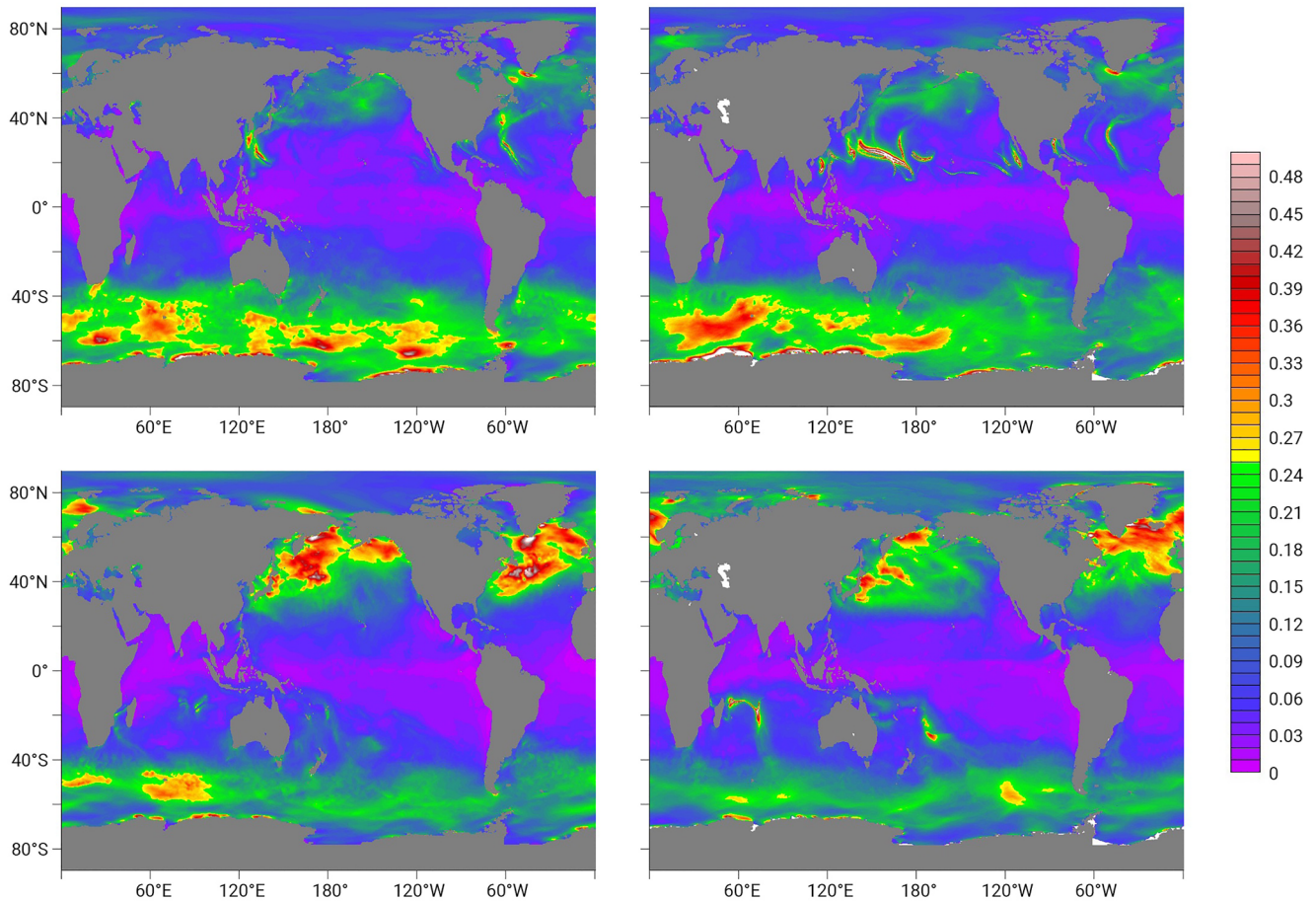
Figure 1. Standard deviations of hourly zonal wind stress based on ERA5 (left) and ICON-ESM (right) for a period of about 40 days. The top panel is for the period 20 August to 30 September and the lower panel is for the period from 20 January to 28 February. The unit is Pa.

values of standard deviations—imprints of tropical cyclones—are abundantly simulated by the ICON model during the 40-day boreal summer period (top right panel of Figure 1), but also found in the ERA5 data (top left panel of Figure 1).

2.2. Analysis Methods

The analysis is carried out for a boreal winter period of 39 days (from 20 January to 28 February), hereafter referred to as the FEB period, and for a boreal summer period of 41 days (from 20 August to September 30), hereafter referred to as the SEP period. Hourly data are stored for the SEP period, whereas only 3-hourly upper ocean data are stored for the FEB period. The difference between the result obtained using 3-hourly output and those from 1-hourly output is small, both with respect to the integral values and the spectra (Appendix A). All output fields have been interpolated onto a regular grid of 0.1°.

The wind power input to near-inertial motions, hereafter referred to as INPUT, is estimated from the covariance $\overline{\tau'_x u'} + \overline{\tau'_y v'}$, where the overbar indicates an average over either the SEP or FEB period, τ'_x and τ'_y are filtered zonal and meridional wind stress and u' and v' are filtered zonal and meridional ocean velocity in the surface layer. The filter retains the spectral power in the frequency band $[0.8f, 1.2f]$, with f being the local Coriolis frequency. This choice could affect the exact value of INPUT.

To estimate the NIW flux radiated from the MLB, we need to first specify the depth of MLB. For that, we take the definition of mixed layer depth (MLD) implemented in the ICON model, which is based on a density threshold. Since we can only perform spectral analysis for variables (e.g., vertical velocity and pressure) at the same level throughout the time, we follow Olbers et al. (2020) and define the MLB as the maximum of the MLD over the

SEP and FEB period, respectively. With this definition, we ensure that our MLB is indeed beneath the mixed layer. We cap the mixed layer at 700 m because the high-frequency output of pressure and vertical velocity is only available in the top 700 m. This, however, covers by far the largest part of the globe. The spatial distributions of the depth of MLB in SEP and FEB are shown in Appendix B.

The NIW flux radiated from the MLB, hereafter referred to as FLUX, is estimated from the covariance $\overline{w'p'}$, where w' is the filtered vertical velocity and p' filtered hydrostatic pressure, both at the MLB. w' and p' are filtered in a way different from u' and τ'_x used for estimating INPUT. Instead of focusing on the near-inertial frequency $[0.8f, 1.2f]$, FLUX is based on the whole super-inertial frequency band containing all frequencies larger than the local Coriolis frequency f. This frequency band is chosen, since the internal waves excited by the winds can have frequencies of multiples of f (Niwa & Hibiya, 1997).

Hereafter, the phrases "INPUT" and "FLUX" are reserved for energy flux contained in the above described frequency bands, whereas the words "input" and "flux" refer, when not specified otherwise, to input and flux without an association with a particular frequency band.

For selected regions, we consider also the co-spectrum $\Gamma_{\tau \cdot \mathbf{u}}$ between wind stress and surface current velocity, the co-spectrum Γ_{pw} between pressure p and vertical velocity w at MLB, and the power spectrum Γ_w of vertical velocity w at MLB. For any two variables, the covariance between them equals the co-spectrum (i.e., the real part of the cross-spectrum) integrated over the entire (positive and negative) frequency domain. Note also that the co-spectrum can be positive and negative. For $\Gamma_{\tau \cdot \mathbf{u}}$ and Γ_{pw}, positive values indicate downward fluxes, and negative ones indicate upward fluxes. In order to focus on NIWs at MLB, we choose to consider the spectrum of vertical velocity, rather than that of horizontal velocity $\mathbf{u}_h$. This is because a large portion of the variability of w is attributed to NIWs, whereas a large portion of the variability of $\mathbf{u}_h$ is attributed to mesoscale motions.

3. Results

3.1. Spatial Distributions and Global Integrals

The wind power INPUT at the sea surface is downward (positive) and reveals large values in the mid-latitude oceans beneath the major synoptic storms, especially strong in the winter hemisphere (Figure 2). Apart from these known features, Figure 2 shows also tracks with high values of INPUT. These tracks correspond to the strong wind stresses associated with tropical cyclones, also visible in the left panel of Figure 1, which are more abundant during the SEP period than during the FEB period. Under a tropical cyclone, the surface INPUT can reach values up to 40–60 mW/m² (contours in Figure 5a). The more zonally orientated tracks, for example, the one near 24°N in the North Pacific during the SEP period, leads to the maximum near 24°N in the latitudinal profile of the zonally integrated INPUT (top left panels in Figure 2). Without tropical cyclones, the zonally integrated INPUT reveals a smooth latitudinal profile with a broad maximum around 40°S–60°S in SEP and 30°N–50°N in FEB.

The NIW FLUX at the MLB (Figure 3) has a spatial distribution similar to that of INPUT, especially with regard to the tracks of tropical cyclones and the higher values in the mid-high latitude oceans. Different from INPUT, which is mainly downward (positive), FLUX can be both downward and upward (positive and negative). The FLUX is however clearly downward under a tropical cyclone, and can reach up to 15–20 mW/m² (color shadings in Figure 5a). Overall, the downward FLUX prevails, leading to positive zonally integrated FLUX at all latitudes (left panel of Figure 3).

The ratio FLUX/INPUT (Figure 4) in the subtropical and tropical oceans is noisy and has a magnitude much higher than one if there is no tropical cyclone, but more homogeneous and around +0.2 to +0.5 if there is a tropical cyclone (Figure 5b). The large noisy values arise from near-zero INPUT, as for example, indicated by the zero contour line off the tropical cyclone track (top panel in Figure 5). In the mid- and high-latitude oceans, the ratio is less noisy and tends to be positive and has a magnitude smaller than one. The large noisy values of FLUX in the tropical and subtropical oceans result partially from the weak wind stress fluctuations there, and partly from the fact that NIWs in the low-latitude oceans are generally stronger than NIWs in the mid- and high-latitude oceans, due to the equatorward propagation of NIWs, an issue to be further discussed in the next subsection.

As shown in Table 1, the global integral of INPUT is about 0.28 TW for SEP and 0.23 TW for FEB, which are close to the lower bound of the previous estimates obtained from km-scale O-GCMs (Flexas et al., 2019; Raja
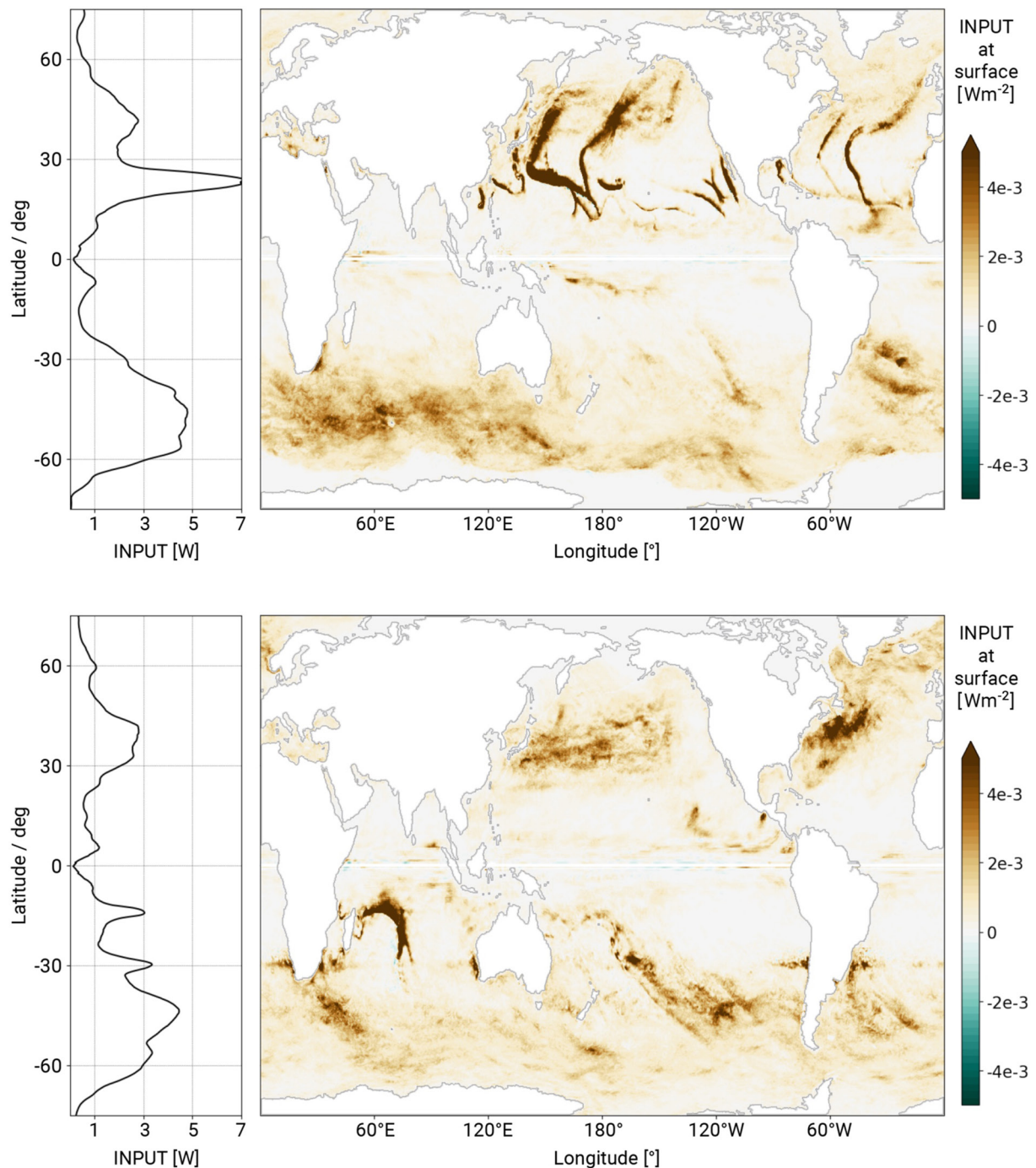
Figure 2. Wind power INPUT to surface currents within the near-inertial frequency range in W/m² (right) and their latitudinal profiles in W (left), obtained by integrating INPUT over zonal bands with width of 0.1°, for the SEP (top) and FEB (bottom) season.

et al., 2022). The globally integrated NIW FLUX at MLB is downward and amounts to about 30% of the globally integrated INPUT for both SEP and FEB periods.

By separating the global domain into a subdomain, over which there is no tropical cyclones during the considered time period, and a subdomain, over which there is at least one tropical cyclone during the considered time period (see Appendix C for the separation method), we can estimate the contributions from TCs to INPUT and FLUX. The result (Table 2) shows the largest TC contribution occurs during the SEP period, the major hurricane season,
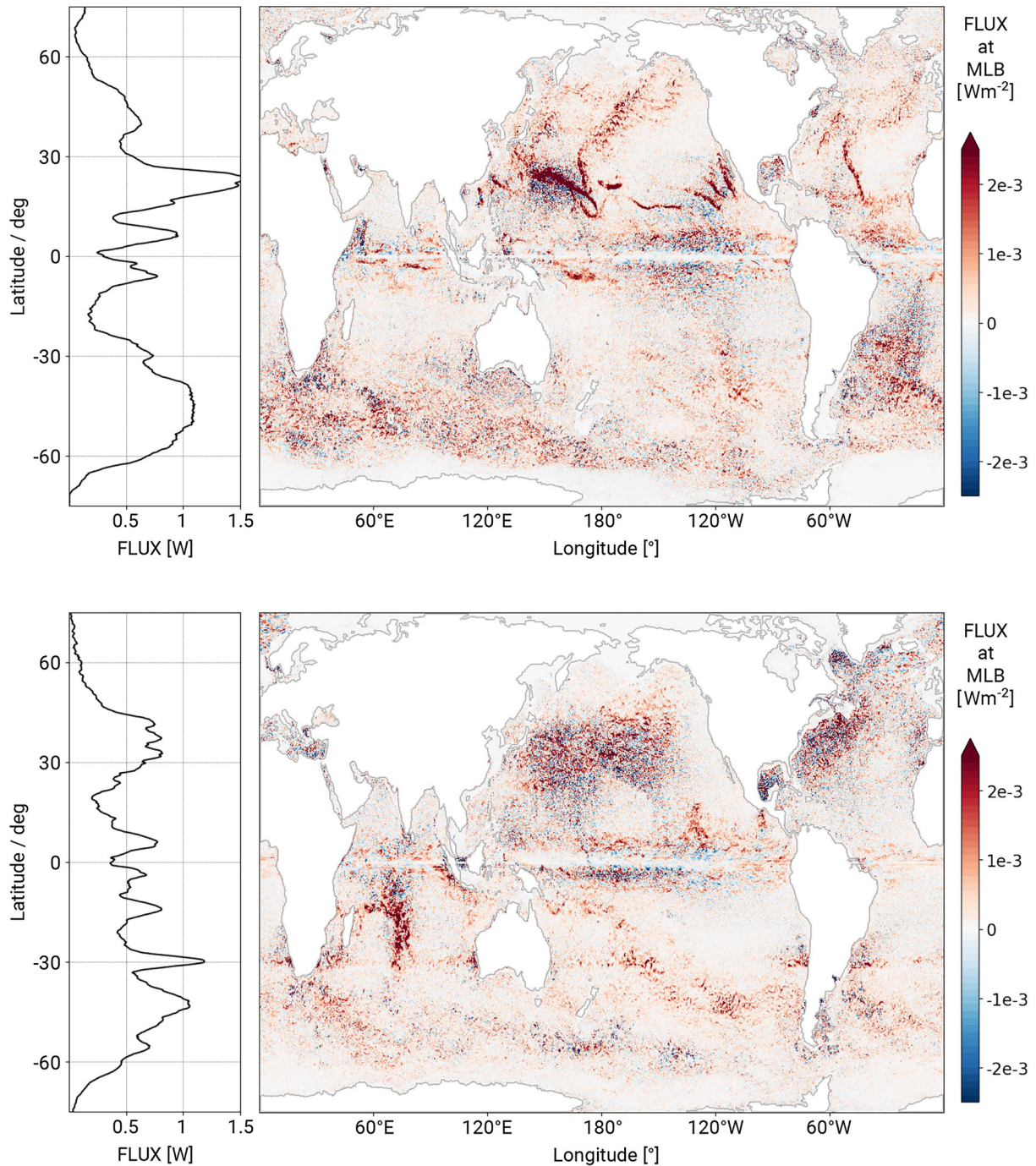
Figure 3. The energy FLUX due to internal waves radiated at mixed layer bottom (MLB) in W/m^2 (right) and their latitudinal profiles in W, obtained from integrating FLUX over zonal bands with width of $0.1°$ (left), for the SEP (top) and FEB (bottom) season.

and amounts to about 38% of the globally integrated INPUT and 77% of the hemispherically integrated INPUT. The TC contribution to FLUX in SEP amounts to about 33% of the globally FLUX and 64% of the hemispherically integrated FLUX. During the FEB period, there are much less tropical cyclones in the southern summer hemisphere. The respective percentages values are more than halved.

The TC contribution to INPUT averaged over the SEP and FEB period is about 0.07 TW, which is larger than the values of 0.03 and 0.05 TW obtained from Liu et al. (2008) and Alford et al. (2016). It is not clear whether the larger value is due to the too crude method used to identify the TC contribution, or to the fact that geostrophic
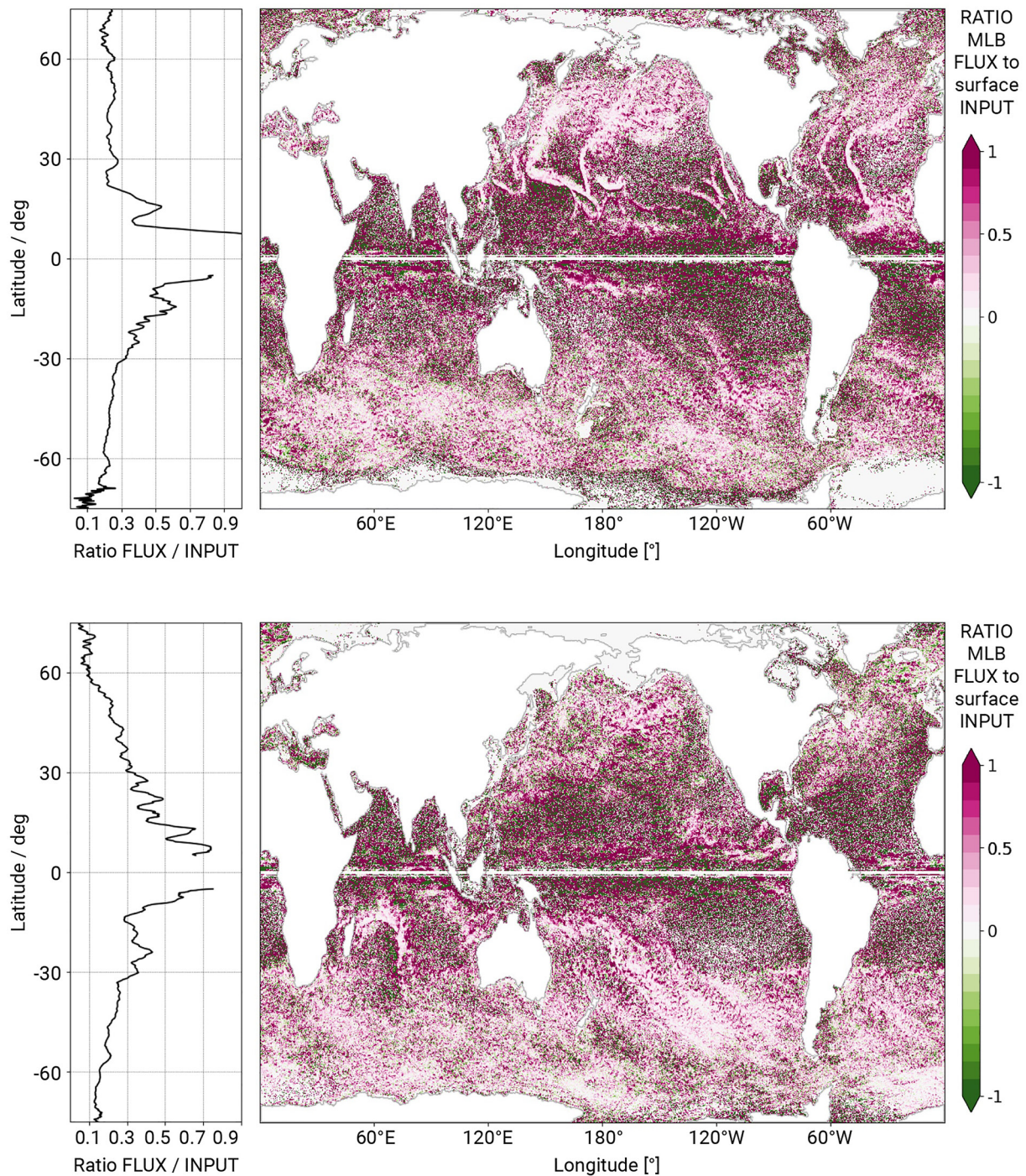
Figure 4. Ratio of the FLUX shown in Figure 3 relative to the INPUT shown in Figure 2.

wind is used to derive the wind stress employed by Liu et al. (2008), or to an overestimation of the intensity/the number of tropical cyclones by the ICON model.

3.2. Case Studies

To better understand how the ocean reacts to the atmosphere simulated by the 5 km ICON model, we examine three cases in more details: Case A and B (Figures 6 and 7) correspond to situations in a subtropical region, one
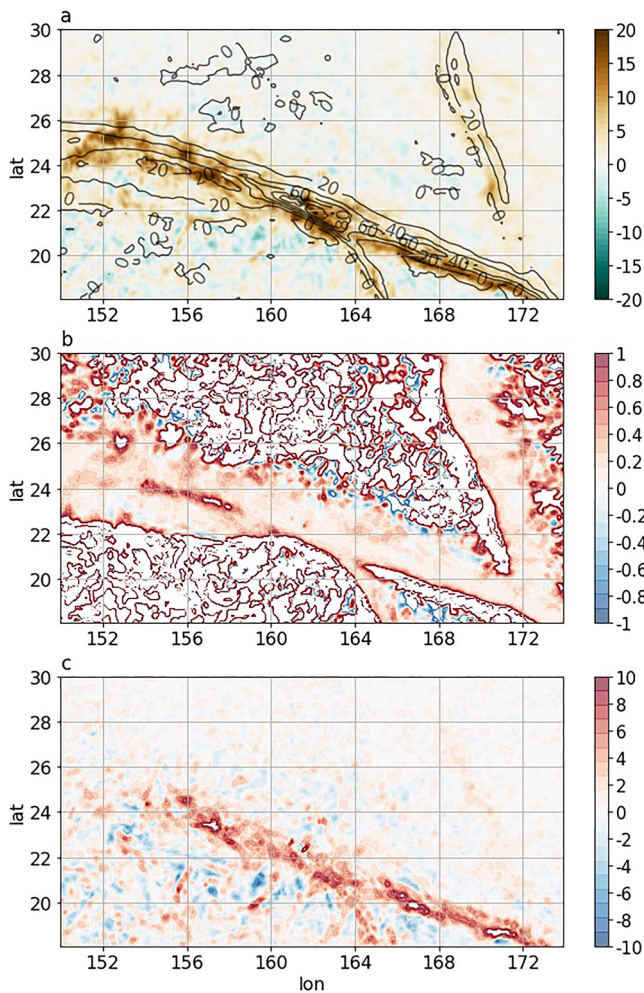
Figure 5. (a) INPUT (contours) and FLUX (shadings), (b) the ratio FLUX/INPUT, and (c) FLUX related to higher harmonics, defined as the difference between the FLUX due to all internal waves and the FLUX due to internal waves within the near-inertial frequency range. All plots are for a box in the North Pacific during the SEP period, where a tropical cyclone (TC) is found. All values of INPUT and FLUX are given in mW/m².

Table 1
Global and Hemispheric Integrals of INPUT, FLUX, and the FLUX-To-INPUT Ratio During the SEP and FEB Period

	SEP			FEB		
	INPUT	FLUX	Ratio	INPUT	FLUX	Ratio
Global	0.277	0.083	30%	0.234	0.071	30%
NH	0.139	0.042	30%	0.085	0.029	34%
SH	0.138	0.04	29%	0.149	0.042	28%

Note. INPUT and FLUX are given in TW, and Ratio in percentage.

with and one without a tropical cyclone. Case C and D (Figures 8 and 9) correspond to (southern) winter-time situations, one with and one without a small mid-latitude storm. The cases cover different types of surface wind stress, namely those around 10 Pa or stronger under a tropical cyclone (Figure 6, top), those up to 0.1 Pa under relatively calm summer-time subtropical weather condition (Figure 7, top), and those about 0.5 Pa under winter-time mid-latitude weather disturbances (top panels in Figures 8 and 9). The ocean responds differently to these different types of wind stress.

In the presence of a TC (Case A, Figure 6), when the wind stress is strong, the ocean evolves as if it is only forced by the wind stress. Directly under the TC, the surface current rotates in a similar way and with a similar spatial scale as the TC, although the center of the circular currents is slightly behind the TC, as can be seen by comparing the center of the rotating currents with the location of the eye of the TC indicated by the small blue circle shown in the bottom panel of Figure 6. Apart from the rotating currents directly below the TC, the currents are stronger to the right than to the left of the TC. The stronger currents, which cover a large portion of the considered domain, are likely caused by the fast movement of the TC, which travels over roughly 100 km northeastward in 6 hr (corresponding about 5 m/s). This traveling velocity is in the direction of the cyclonic winds to the right of the TC, but in the direction opposing the cyclonic winds to the left of the TC. The wind stress is hence stronger and leads to stronger surface current to the right than to the left of the TC in the direction of the TC movement. Also shown in Figure 6 is the vertical velocity at the MLB (color shadings in the bottom panel). Different from the surface horizontal current, which comprises mainly forced motions and the mesoscale and sub-mesoscale motions, the vertical velocity w at MLB comprises to a large extent free wave motions. We find that w is downward in the front of the eye of the TC and upward behind eye of the TC. This structure of vertical velocity moves with the TC.

In the absence of a TC and in the summer-time subtropical ocean (Case B, Figure 7), when the wind stress is weak, the surface current does not necessarily flow in the direction of the wind stress. In the lower left part of the considered domain, wind stresses are weak, but surface currents are strong. In the upper right part of the considered domain, wind stresses are strong, but surface currents are weak. At the two considered time instances, the surface current structure is characterized by the same eddy west of about 162.5°E, while the wind stress undergoes noticeable changes. At the second time instance (right), the wind stress reveals small-scale divergence, likely related to small convective events. There is no indication that surface currents respond to these bursts of wind stresses. On the contrary, we observe situations, for example, at the second instance near 23°N, 161.5°–162°E, where the surface current flows in the direction opposite to that of the wind stress. There, the stress will damp, rather than reinforce, the surface current. Different from the surface current, which has the imprint of an mesoscale eddy and does not vary much in 8 hr, the vertical velocity at the MLB reveals quite different distributions at the two considered time instances, indicative of fast wave motions.

Under the winter-time mid-latitude weather disturbances (Case C, Figure 8), when eastward wind stress prevails, surface current tends to have an eastward component. On top of this forced eastward tendency, the surface current reveals also strong self-reinforced tendencies, characterized by meandering and eddying structures, in stark contrast to the more or less uniform spatial distribution of the wind stress. The current structure remains essentially the same within the 8 hr. Different from the inert surface current, the vertical velocity (color shadings in the bottom panel) changes drastically within 8 hr.

Table 2
Portions of the INPUT and FLUX, That Are Induced by Tropical Cyclones

	SEP		FEB	
	INPUT	FLUX	INPUT	FLUX
Global TCs	0.106 (38%)	0.027 (33%)	0.032 (14%)	0.011 (15%)
NH TCs	0.106 (77%)	0.027 (64%)	0.0 (0%)	0.0 (0%)
SH TCs	0.0 (0%)	0.0 (0%)	0.032 (21%)	0.01 (24%)

Note. Numbers given without brackets are in TW, and numbers in brackets are percentages due to TCs.

Under winter-time mid-latitude weather disturbances, we find also occasions, where the ocean barely responds to wind stress. In Case D (Figure 9), a small storm (diameter of about 300 km) is passing through the considered domain from left to right within 8 hr. The surface currents meander seemingly unaffected by the passing storm. When looking closely, we see a slight eastward movement of the meandering current pattern during the 8 hr, which likely is related to the overall eastward moving wind system. At the instance shown in the right column of Figure 9, the wind stress barely inputs any power into the surface current. The strong wind stress south of 45°S near 62°E−63°E has a large component in the direction opposed to that of the surface current. These stresses will damp, rather than reinforce, the surface currents.

The wind stresses shown in the top panels of Figures 7 and 9 arise from less-extreme short-living weather disturbances. The surface currents do not noticeably respond to these wind stresses and continue to flow in the way before the onset of the weather disturbances. The ICON model with its 5-km resolution and 15-min coupling frequency likely resolves more and passes more such small-scale short-living atmospheric disturbances to an ocean than a lower resolution model does. For a strongly eddying ocean simulated by the 5 km ICON model, these wind stresses may be too weak to steer the surface currents. We come back to this point in the next section.
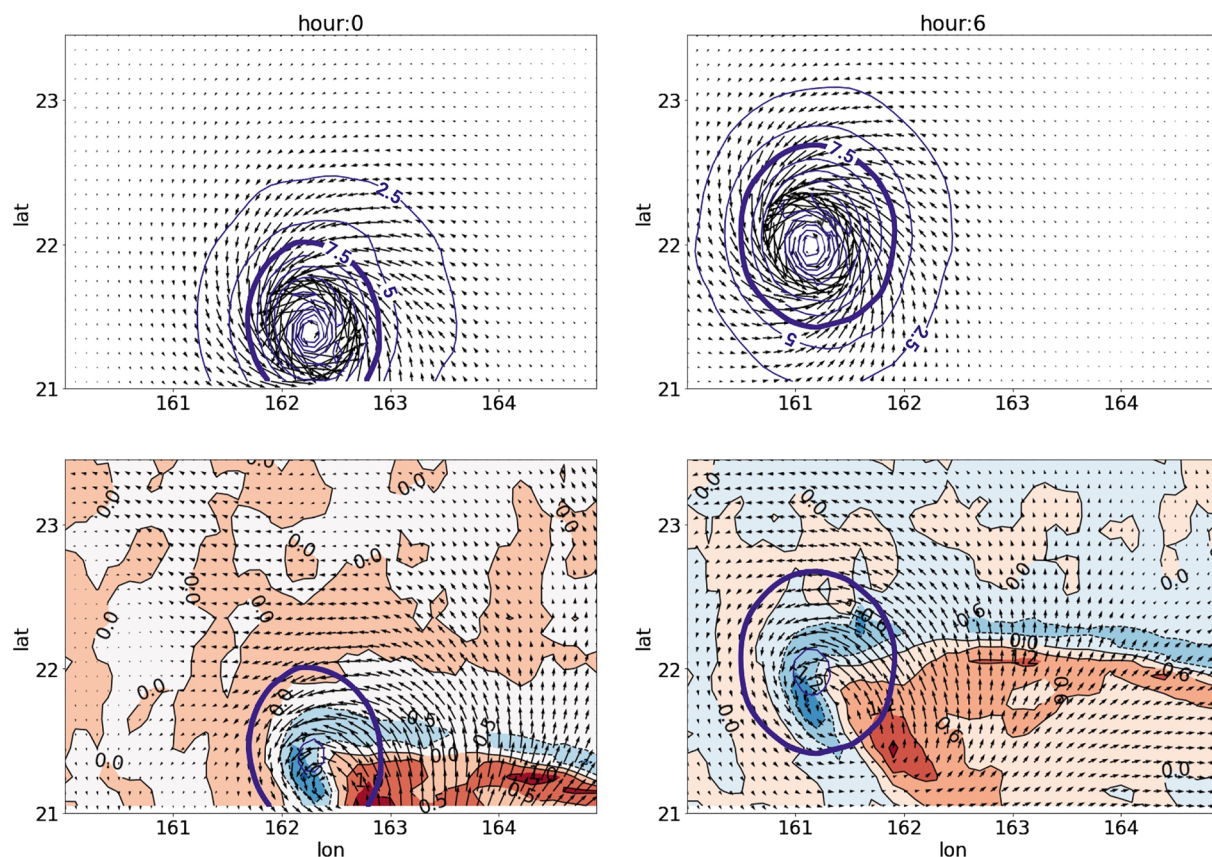

Figure 6. Surface wind stress vectors (arrows in the top panel) and surface current vectors and vertical velocity at mixed layer bottom (MLB) (arrows and color shadings in the bottom panel) at two time instances (left and right). The magnitude of wind stress vector (in Pa), as indicated by the blue contour lines in the top panel, first increases and then decreases toward the eye of the tropical cyclone (TC), and essentially vanishes inside the eye. The thick blue line indicate the 7.5-Pa isoline and marks the position of the tropical cyclone. Vertical velocity at MLB (downward velocities in blue) is in mm/s. The two time instances are 6 hr apart in the SEP period.
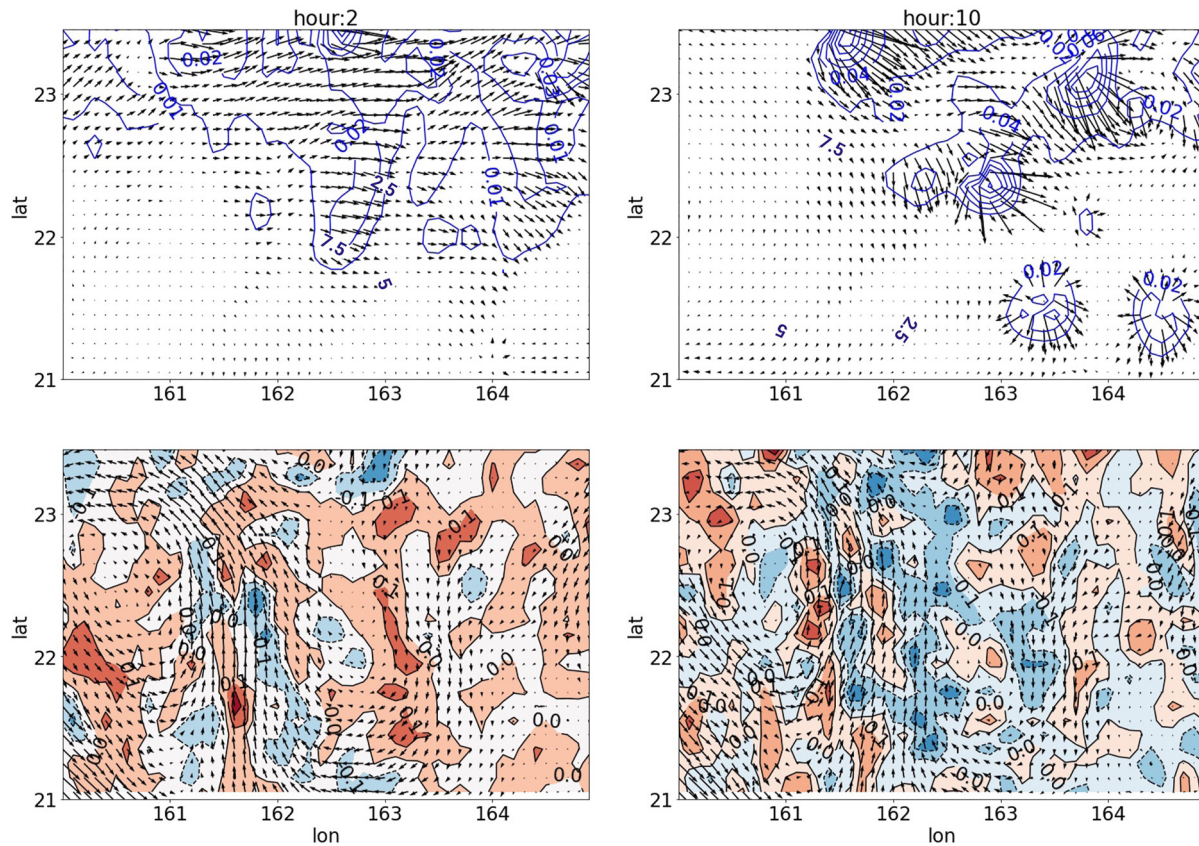
Figure 7. Same as Figure 6, for the same region but at two time instances when there is no tropical cyclone in the SEP period. The right panel is 8 hr after the left panel.

3.3. Spectral Behaviors

We examine spectra derived from a small region in the North Pacific, in which a tropical cyclone is found during the SEP period. The results are by and large representative for other regions with a TC (not shown). We consider (a) the co-spectrum $\Gamma_{\tau \cdot \mathbf{u}}$ that characterizes the wind-power input at the surface, (b) the co-spectrum Γ_{pw} that characterizes the flux radiated at MLB, and (c) the power spectrum Γ_w of vertical velocity w at MLB that characterizes the waves generated at the MLB.

We examine first the spectral behaviors at, and south and north of, 24°N, the latitude that corresponds roughly to the center of the TC track extending from 150°E to 160°E during the SEP period. Figure 10 shows for the SEP period, $\Gamma_{\tau \cdot \mathbf{u}}$ (top), Γ_{pw} (middle), and Γ_w (bottom), estimated as averages of periodograms at grid points in latitudinal bands centered at 24°N, 20°N, and 16°N (left), and at 30°N, 35°N, and 40°N (right). Each of the bands contains 102 grid points. The vertical dashed lines indicate the local Coriolis frequency f and the vertical dotted lines $2f$ at these latitudes. For $\Gamma_{\tau \cdot \mathbf{u}}$ and Γ_{pw}, positive values (downward fluxes) are indicated by crosses, and negative values (upward fluxes) by dots.

At the latitude of the tropical cyclone (i.e., at 24°N), $\Gamma_{\tau \cdot \mathbf{u}}$ (red symbols in Figure 10a) is essentially downward and peaks at frequencies slightly higher than the Coriolis frequency f_{24} at 24°N (red dashed lines in Figure 10a). Γ_{pw} (red symbols in Figure 10c) peaks not only at the local Coriolis frequency f_{24}, at which $\Gamma_{\tau \cdot \mathbf{u}}$ has a distinct spectral maximum, but also at $2f_{24}$, at which $\Gamma_{\tau \cdot \mathbf{u}}$ does not show a distinct spectral maximum. Generally, there is a tendency for tropical cyclones to excite NIWs at higher harmonics. This tendency is more clearly shown by Γ_w (red line in Figure 10e).

For $\Gamma_{\tau \cdot \mathbf{u}}$ away from the latitude of the tropical cyclone, the spectral level is noticeably lower than that at 24°N, indicating a strong reduction of wind power input away from the strongest input directly under a tropical cyclone. South of 24°N (blue and green symbols in Figure 10a), $\Gamma_{\tau \cdot \mathbf{u}}$ does not reveal a clear peak at the local Coriolis
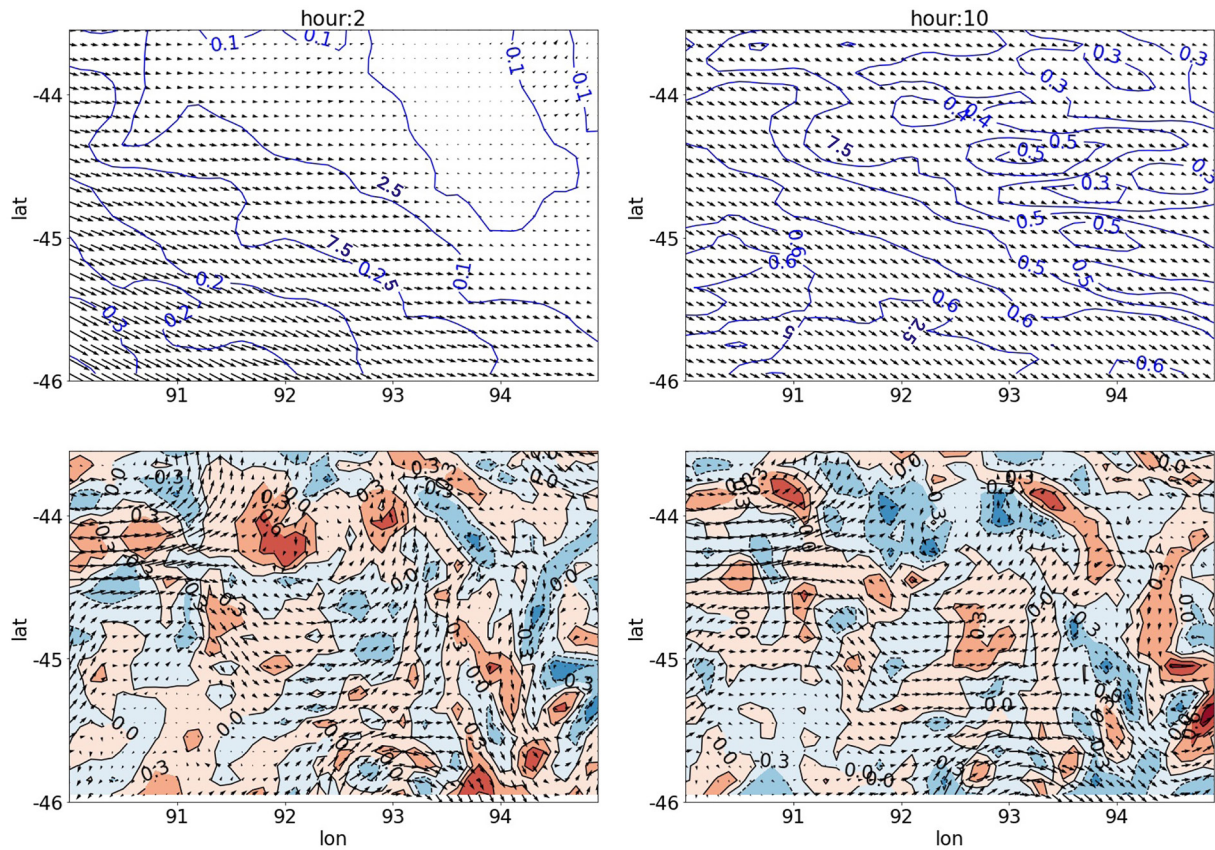
Figure 8. Same as Figure 6, but for a region in the southern Indian Ocean at two time instances in the SEP period during the southern winter. The right panel is 8 hr after the left panel.

frequency (blue and green dashed lines), and is occasionally upward. North of 24°N (all symbols in Figure 10b), $\Gamma_{\tau\cdot\mathbf{u}}$ peaks at the local Coriolis frequency, and is essentially downward.

For Γ_{pw} away from the latitude of the tropical cyclone, quite different behaviors north of and south of 24°N are found. South of 24°N (blue and green symbols in Figure 10c), Γ_{pw} peaks at the frequency near f_{24N}, as well as at the frequency near $2f_{24N}$ (indicated by the red vertical lines), but not at the respective local Coriolis frequencies (indicated by the blue and green dashed lines). North of 24°N (all symbols in Figure 10d), Γ_{pw} do peak at the respective local Coriolis frequency. The peaks in Γ_{pw} are noticeably broadened relative to those in $\Gamma_{\tau\cdot\mathbf{u}}$.

The above-described features of Γ_{pw} can be more clearly seen from the power spectrum of vertical velocity Γ_w: the spectra Γ_w at 20°N and 16°N (blue and green lines in Figure 10e) peak at the same frequencies as Γ_w at 24°N (red line in Figure 10e), namely close to f_{24}, $2f_{24}$ and $3f_{24}$ (red vertical lines), rather than at the local Coriolis frequency (blue and green vertical lines). On the other hand, the spectra Γ_w at 30°N, 35°N, and 40°N peak near the local Coriolis frequencies (vertical lines in Figure 10f). Furthermore, the spectral peaks of Γ_w are much broader north of 24°N than south of 24°N.

To understand these behaviors, recall that a NIW move mostly equatorward because of the turning point located poleward of the generation latitude of the NIW. Thus, NIWs at a latitude should be considered as consisting of both NIWs, that are locally generated, and NIWs, that are generated farther poleward and propagated into the considered latitude. The tropical cyclone at 24°N induces strong inertial currents, whose divergence excites strong NIWs. These waves propagate from their generation site at 24°N southward, thereby retaining not only their frequency but also most of their strength, even 8° (~800 km) south of the generation latitude. The conservation of their original frequency is further favored by the weak wind-forcing south of the tropical cyclone. In this sense, the co-spectrum Γ_{pw} and the spectrum Γ_w at 16°N and 20°N (blue and green in Figures 10c and 10d) contain essentially only contributions from NIWs generated by the tropical cyclone at 24°N.
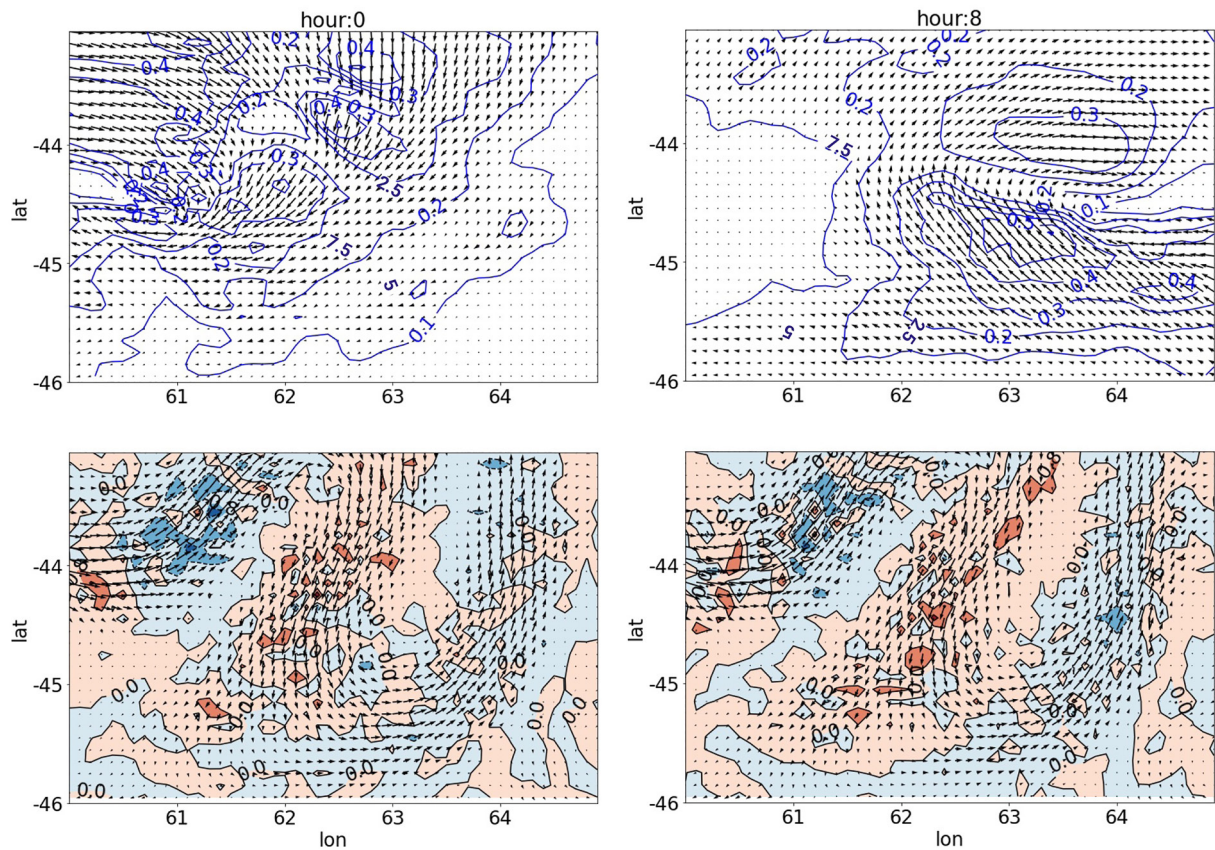
Figure 9. Same as Figure 6, but for a region in the southern Indian Ocean at two time instances in the SEP period during the southern winter. The right panel is 8 hr after the left panel.

In the absence of tropical cyclones, such as north of 24° or during the FEB period (Figure 11), the fluxes at MLB contain both NIWs that are locally generated and NIWs that are generated further poleward. As a result, the spectral peaks in Γ_{pw} and in Γ_w are located near the local Coriolis frequency and are broad toward higher frequencies. The broadening results from waves generated farther poleward that have higher frequencies. When considering a width of the spectral maximum as a measure of the contribution from remotely generated NIWs, the broader spectral maxima at lower latitudes (Figure 11e) relative to those at higher latitudes (Figure 11f) indicate that the contribution from the remotely generated NIWs increases with decreasing latitude. The spectral maxima are at frequencies much higher than the local Coriolis frequency at 16°N and 24°N (Figure 11) than the maxima at 30°N, 35°N, and 40°N do. This is also true for the secondary maxima at near multiples of the local Coriolis frequency.

The co-spectra $\Gamma_{\tau \cdot u}$ and Γ_{pw} reveal not only downward fluxes (marked by crosses). Upward fluxes (marked by dots) are also present, especially for the flux at the MLB. Olbers et al. (2020) attribute the upward fluxes to nonlinear interactions of directly wind-forced NIWs, by which energy is redistributed/converted from NIWs at near-inertial frequency to its higher harmonics. If this conversion occurs farther deeper below the ML, upward flux at higher harmonic frequencies can be found at the MLB. We notice that there are much less upward fluxes directly beneath the tropical cyclone at 24°N than south of the tropical cyclone (compare red and blue symbols in Figure 10c).

The wind-power input at the surface is clearly downward when integrated over the entire near-inertial frequency range [0.8f, 1.2f], as indicated by Figure 2. When decomposed into different frequencies, $\Gamma_{\tau \cdot u}$ can also be upward occasionally, especially under a weak wind-forcing, for example, at low latitudes (blue and green dots in Figure 10a and the dots in Figure 11a). In this case, surface currents are affected more strongly by oceanic internal instability processes that produce mesoscale eddies, than by the imposed wind stress. We return to this point in the next section.
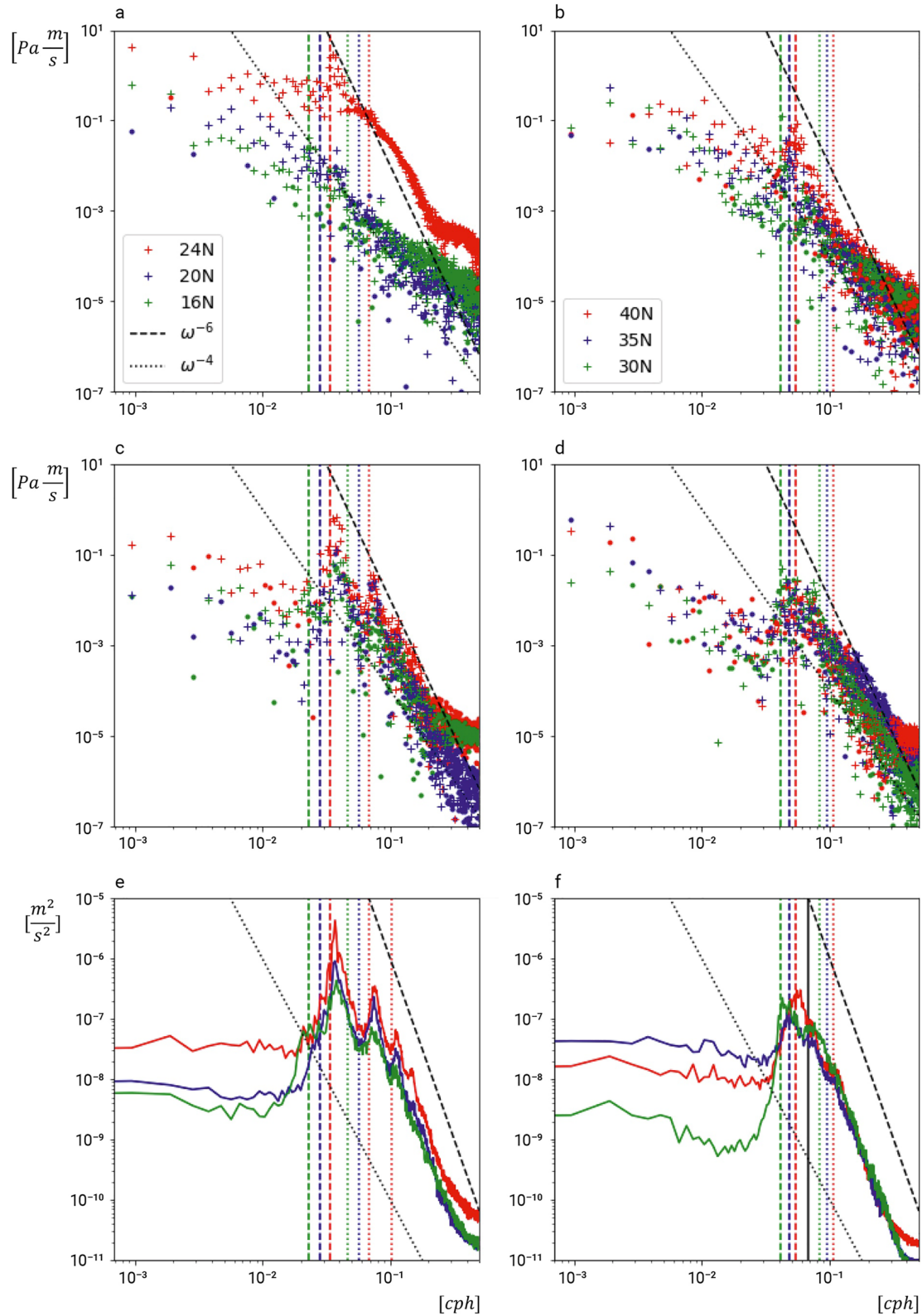
Figure 10.

4. Discussion

4.1. Sensitivity of Wind-Power INPUT

Using a one-dimensional model, Klein et al. (2004) and Klein (2008) found a loss of about 20% in near-inertial energy when using 6-hourly winds instead of 3-hourly winds. Rimac et al. (2013) showed a similar sensitivity that the globally integrated INPUT increases from 0.3 TW to 1.1 TW when replacing 6 hourly wind forcing by 1 hourly wind forcing. We hence expected a further increase in the globally integrated INPUT from the ICON-simulation, as a coupling frequency of 15 min is used in the simulation. Contrary to this expectation, the globally integrated INPUT amounts barely 0.3 TW.

Below we discuss three factors that can act to reduce the INPUT. The first factor is well known. Different from Rimac et al. (2013), which assumes an ocean at rest, the wind stress in the ICON model is derived from a bulk formulation that accounts for the surface current velocity. Previous studies (Dawe & Thompson, 2006; Eden & Dietze, 2009) showed that such a wind stress formulation leads to a reduction of the total wind-power input compared with the formulation that ignores surface current. For the wind power input into the near-inertial frequency band, the reduction can reach about 20%–25% (Rath et al., 2013; Zhai, 2017).

The second factor is the asymmetry of the role of the wind stress in positively and negatively forcing the ocean, identified when the wind stress is formulated as being proportional to wind velocity relative to current velocity. Renault et al. (2016) and Rai et al. (2021) pointed out that the negative wind work (or damping) exerted by a wind stress in the direction opposite to a surface current is stronger than the positive wind work exerted by a wind stress in the direction of a surface current (assuming the wind stress and surface current having the same magnitudes in the two directionally different configurations). Thus, when *spatially* average over a large-scale wind stress over an eddy, the net effect is a damping, leading to the so-called eddy killing process. We speculate that the asymmetry can also lead to a net damping when averaged *temporally*. Section 3.2 shows that under weak weather disturbances simulated by a 5 km ICON, the surface current can be in the same or the opposite direction of the wind stress. Assuming a normally distributed alignment between wind stress and surface current, the asymmetry described by Renault et al. (2016) and Rai et al. (2021) can also give rise to a net damping when averaged temporally, inducing a lower wind input. A random alignment is expected when surface currents are more strongly determined by the internal instability processes than by the external wind stresses. So far, the damping (eddy killing) effect applies to the total wind input. Further investigation is required to quantify the damping effect on the INPUT at near-inertial frequencies.

The third factor is the ocean model used for deriving the INPUT. While there are several studies addressing the sensitivity of INPUT to the wind stress used (Jiang et al., 2005; Rimac et al., 2013), we are not aware of any studies addressing the sensitivity of INPUT to the ocean model used. We believe that the choice of the ocean model, which needs to be made due to the lack of current observations, can also have a noticeable impact on the INPUT. Many of the previous works (Alford, 2001, 2003b; D'asaro, 1985; Jiang et al., 2005; Watanabe & Hibiya, 2002) rely on a slab model from Pollard and Millard (1970). Within this model, the ocean is directly forced by the wind stress. A slab ocean differs from an ocean simulated by a km-scale O-GCM. While the currents of a slab ocean are always directly linked to the applied wind stress, the surface currents in a km-scale O-GCM can result not only from the wind stress forcing but also from internal instability processes, which generate among other mesoscale eddies. The exclusive role of wind stress in generating the currents in a slab ocean can lead to an overestimation of the ocean's response to the wind stress.

Apart from slab model, previous studies also use O-GCMs for estimating INPUT. However, the simulations performed usually hardly resolve any mesoscale eddies. For instance, Rimac et al. (2013) uses an O-GCM that has a horizontal resolution of 0.4°, which is too coarse to resolve the full eddy field. Furuichi et al. (2008) uses an O-GCM having a much higher horizontal resolution (0.15° × 0.125°). However, their simulations start from an oceanic state restored to climatological non-eddying temperature and salinity fields. Such a state does not contain any mesoscale eddies. Different from Furuichi et al. (2008), the ocean of the 5 km ICON-O has a well-established

Figure 10. Co-spectrum $\Gamma_{\tau \cdot \mathbf{u}}$ at the sea surface (top), co-spectrum Γ_{pw} at the mixed layer bottom (MLB) (middle), and spectrum Γ_w at the MLB (bottom) during the SEP period in zonal bands at latitude $\phi = 16°N$, $20°N$, $24°N$ (left) and at latitude $\phi = 30°N$, $35°N$, $40°N$ (right). The bands have a latitudinal extent from $\phi - 0.1°$ to $\phi + 0.1°$ and a longitudinal extent from $150°E$ to $155°E$ in the left panel, and from $155°E$ to $160°E$ in the right panel. The colors correspond to the latitudes given in the legend. For the co-spectra, positive values are denoted by crosses and negative ones by dots. The dashed vertical lines indicate local Coriolis frequency f and the dotted vertical line $2f$. The black vertical line in (f) indicates $2f_{24°}$ with $f_{24°}$ being the Coriolis frequency at $24°N$.
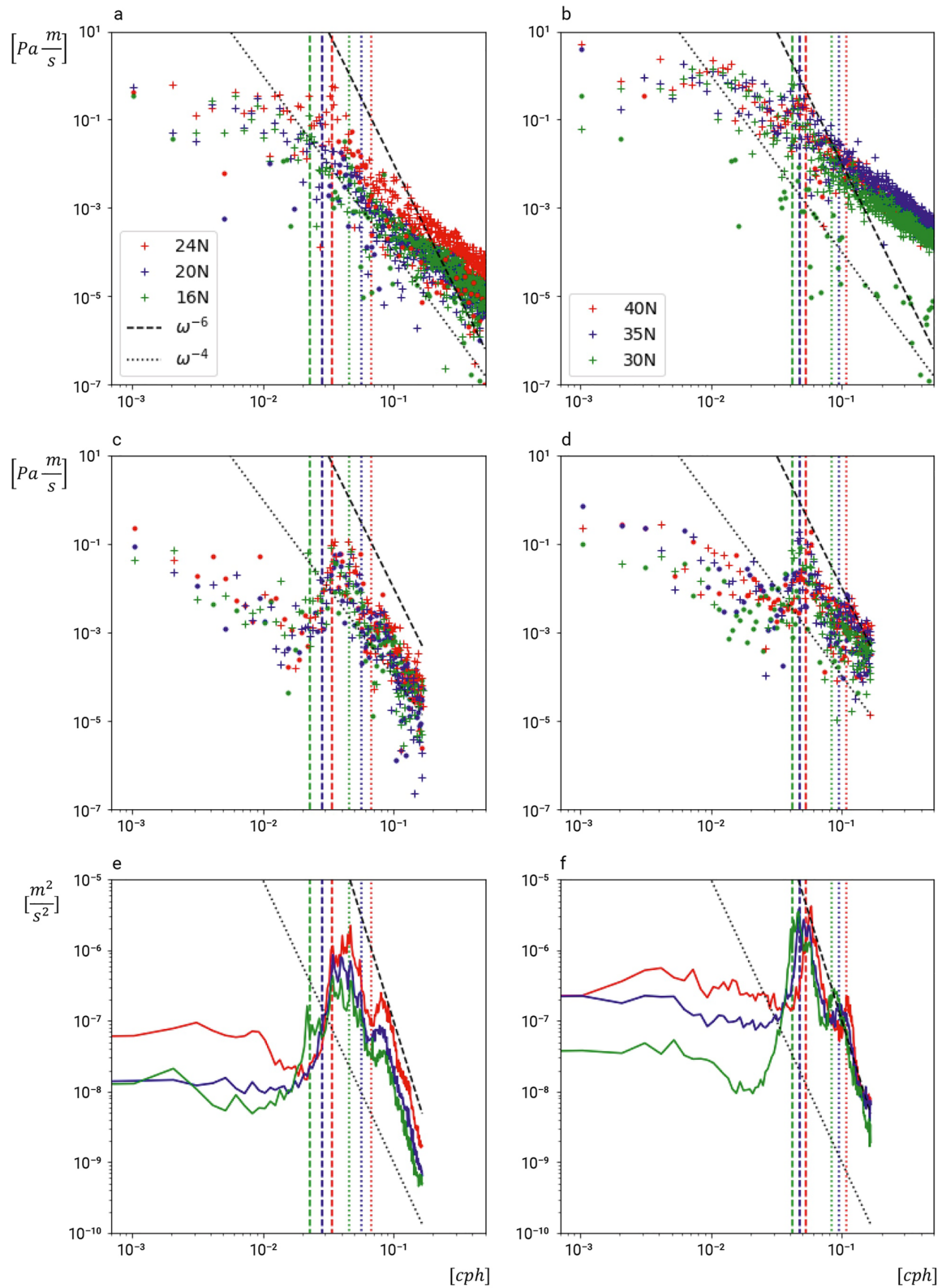
Figure 11. Same as Figure 10, but for the FEB period.

eddy field, due to the long spin-up phase. The surface currents simulated by the 5 km ICON model contain a strong eddying component that is not directly linked to the wind stress forcing, especially when the wind stress forcing is induced by less-extreme small-scale short-living weather disturbances, rather than by TCs. We can easily identify situations where the surface currents continue to flow in the same way as it did before the onset of a less-extreme weather disturbance. The situations shown in Figures 7–9 found in the 5 km ICON simulation can probably not be so easily found in a slab ocean or a non-eddying ocean. The weak wind stress related to less-extreme weather disturbances together with the strong internally generated eddies favor a random alignment of wind stress with surface current, and with that a lower wind input. Flexas et al. (2019) and Rai et al. (2021) found strong dependence of wind input on spatial scales. Further investigation is required to quantify how much the random alignment induced by strong internal ocean dynamics reduces the near-inertial INPUT.

We speculate that the second and the third factor work together to make a high-resolution coupled GCM to produce a lower INPUT. The speculation is in line with the low INPUT of about 0.16 TW obtained from a 1/48° simulation with the GMTgcm (Flexas et al., 2019) and the INPUT of about 0.21 TW obtained from a 1/25° simulation with HYCON (Raja et al., 2022). Flexas et al. (2019) suggest that wind variability on time scales less than 6 hr and spatial scales less than 15 km are critical to better representing (i.e., obtaining higher value of) the wind power input in ocean circulation models. Based on our above consideration, we suggest that the low value obtained by Flexas et al. (2019) likely results from an ocean with strong mesoscale and sub-mesoscale eddies that emerge largely independent of the wind forcing.

4.2. Superinertial NIWs Generated by a Tropical Cyclone

Using an idealized ocean model forced with steady wind stress from a tropical cyclone, Niwa and Hibiya (1997) showed that tropical cyclone excites internal waves not only at the near-inertial frequency f, but also at superinertial frequencies $2f$ and $3f$ due to nonlinear wave interactions. The coupled ICON simulation configured in a realistic setting confirms the TC-induced $2f$ and $3f$ internal waves (Figure 10e). We further quantify the contribution from the superinertial internal waves to the MLB FLUX by calculating the difference between the MLB FLUX arising from all resolved internal waves (i.e., with frequency larger than f) and the MLB FLUX arising from NIWs (i.e., with frequencies in the range $[0.8f, 1.2f]$). Within a TC track, this superinertial contribution reaches up to 10 mW/m² (bottom panel in Figure 5c). Integrated globally, the superinertial contribution amounts to about 10% of globally integrated FLUX for the SEP period.

The TC-induced superinertial waves propagate not only equatorward, as shown by the power spectra of vertical velocity (blue and green lines in Figure 10e). About 600 km north of the tropical cyclone at 24°N, that is, at 30°N, the power spectrum of vertical velocity (green line in Figure 10f) shows a broad maximum around the double-inertial frequency at 24°N (black vertical line), the latitude of the tropical cyclone. This suggests a northward propagation, consistent with the study by Niwa and Hibiya (1997).

4.3. More on the Ratio FLUX/INPUT

The new parameterization of oceanic internal waves IDEMIX (Internal Wave Dissipation, Energy and Mixing) (Eden & Olbers, 2014; Olbers & Eden, 2013) requires an accurate estimate of the main wave sources. In the upper ocean, the true wave source is the near-inertial FLUX at MLB, rather than the wind-power INPUT at the surface. However, the FLUX at the MLB is much more difficult to obtain than the surface INPUT. One way to incorporate the FLUX at MLB into IDEMIX without explicitly specifying the FLUX at MLB is to infer the FLUX at MLB from the wind-power INPUT based on our knowledge about the ratio FLUX/INPUT.

For this purpose, information about systematic behaviors of the ratio is valuable. Despite the complex geographical distribution of the ratio FLUX/INPUT, regarding to both the magnitude and the sign of the ratio, we are able to identify two systematic behaviors of the ratio after applying some averaging and aggregation.

First, when zonally integrated, both the INPUT at the surface and the FLUX at MLB are clearly downward (left panels in Figures 2 and 3). Their ratio tends to increase toward the equator (left panel in Figure 4). This latitudinal variation of the ratio is a direct consequence of equatorward propagation of NIWs generated at higher latitudes. In the winter hemisphere, where NIWs at MLB are generated by the usual weather disturbances at mid- and high-latitudes without tropical cyclones, the increase of the ratio with decreasing latitude is by and large
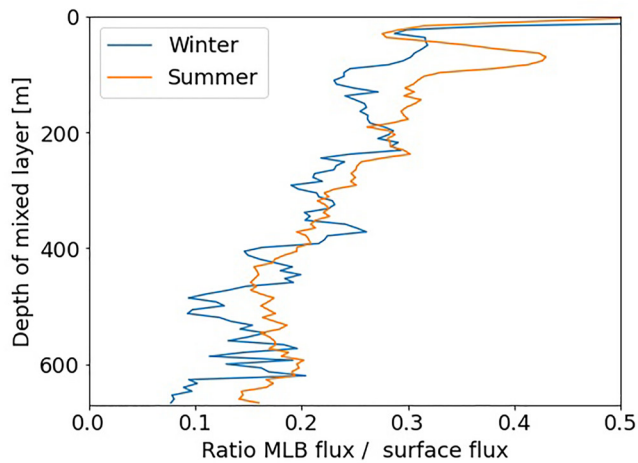
Figure 12. The FLUX-to-INPUT ratio as a function of the depth of mixed layer bottom (MLB), obtained by summing up FLUX and INPUT at grid points with the same mixed layer depth.

monotonous (see e.g., the ratio over the northern latitudes shown in the lower left panel of Figure 4). In the summer hemisphere, where NIWs at MLB are generated in addition to the weather disturbances at mid- and high-latitudes occasionally by tropical cyclones, the increase of the ratio with decreasing latitude is less monotonous.

Second, when summing over grid points having MLB at the same depth, the ratio of the FLUX at MLB to the surface INPUT tends to decrease with increasing MLD (Figure 12). This behavior is consistent with the linear model considered by Olbers et al. (2020), which predicts a decrease of FLUX at MLB with increasing MLD.

Averaged globally, the ratio FLUX/INPUT amounts to about 30%, which roughly doubles the previous estimates of 11% provided by Rimac et al. (2016) using a global model and 17% by Olbers et al. (2020) using a model for the Atlantic. The larger ratio found in this study can be attributed to the strong internal wave activity, which is clearly favored by the tropical cyclones, but may also be favored by the high horizontal and vertical resolution within the mixed layer simulated by the ICON model.

The globally integrated ratio and the dependence of the ratio on latitude and MLD can be used to construct a more accurate surface wave source for IDEMIX without directly calculating the FLUX at MLB.

5. Summary

We re-examine the wind power input at the sea surface (INPUT) and the energy flux due to NIWs radiating away from the MLB into the ocean interior (FLUX) based on a 5 km coupled ICON simulation. The ICON model is capable of resolving tropical cyclones and less-extreme small-scale short-living weather disturbances in the atmosphere and mesoscale and partially sub-mesoscale eddies in the ocean.

We find that the global integrals of INPUT of about 0.23–0.27 TW (depending on season) are near the lower bound of the previous estimates. The previous estimates, which is around 0.5 TW and can amount to more than 1 TW, are derived either from a slab ocean model of Pollard and Millard (1970) or an O-GCM that does not simulate vigorous mesoscale eddies. The surface current in such an ocean is to a large extent slaved to the wind stress forcing, suggesting that using a non-eddying ocean can lead to an overestimate of the wind input to near-inertial motions.

We find also that our global integral of FLUX is about 30% of the INPUT. The ratio almost doubles the previous estimates (11% in Rimac et al. (2016) and 17% in Olbers et al. (2020)). The strong FLUX is related to strong internal wave activity that is caused mainly by the tropical cyclones, but may also be favored by a high vertical resolution within the mixed layer in the ICON model. However, since the total INPUT is low, the ratio of 30% does not prevent that the total FLUX at MLB is well below 0.1 TW, suggesting a weak wind-induced wave energy source.

Relative to the INPUT at the surface, the FLUX at the MLB is more important for the ocean circulation and should be considered as the internal wave source needed for internal wave parameterization like IDEMIX (Eden & Olbers, 2014; Olbers & Eden, 2013). However, the FLUX at MLB is also much more difficult to specify and eventually be implemented in IDEMIX. On the other hand, the FLUX at the MLB can be inferred from the INPUT based on the general features of the FLUX-to-INPUT ratio. We find that the FLUX-to-INPUT ratio tends to decrease with latitude and decrease with MLD. These features can be used to represent the FLUX in IDEMIX solely based on more easily accessible surface properties (surface wind stress). At the same time, our study is a step forward as compared to the recently used globally constant FLUX-to-INPUT ratio (Jochum et al., 2013). A constant FLUX-to-INPUT ratio appears inappropriate, based on Figures 4 and 5.

Finally, we show that the 5 km coupled ICON simulation produces features of wind-induced internal waves consistent with the previous studies. These features include (a) the excitation of strong internal waves under a tropical cyclone that have frequencies not only close to the local Coriolis frequency f, but also at higher harmonics of $2f$ and $3f$, (b) equatorward propagation of these waves over distance as large as 800 km, during which the

original frequencies are preserved, (c) some poleward propagation of the higher harmonics at $2f$, and (d) the general equatorward propagation of the internal waves excited by wind stress arising from mid- and high-latitude weather disturbances, resulting in a broadening of the near-inertial maximum in the wave (vertical) kinetic energy spectrum. We believe that this is the first time that these wind-induced wave properties are reported using a global km-scale coupled atmosphere-ocean GCM.

Appendix A: Effect on Sampling Frequency on Wind Forcing Quantities

Due to the limited storage, we were only able to store 3-dimensional variables (for the upper 700 m) hourly for the SEP period but 3 hourly for the FEB period. We assess the impact of the lower sampling frequency in the winter data by down-sampling the 1-hourly SEP data to 3-hourly data. For the global integrals, the sampling effect is about 5%, larger at high latitudes but almost absent at low latitudes and near the equator (not shown). For the spectra, Figure A1 shows that down-sampling does not noticeably affect the spectral shape and spectral level, albeit that the spectrum derived from 3-hourly data does not resolve frequencies higher than 1/6 cycles per hours.
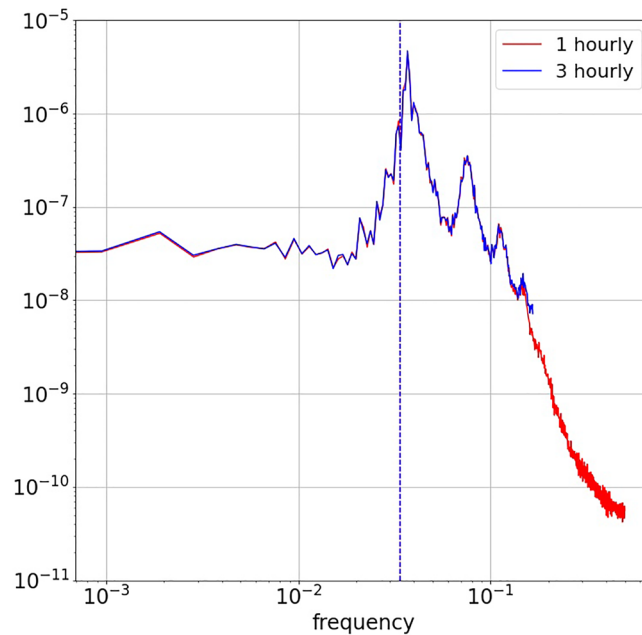

Figure A1. Power spectra derived from hourly (red) and 3-hourly (blue) vertical velocity for the SEP period. The 3-hourly velocity is obtained by down-sampling the hourly velocity. Both spectra are estimated as averages over 102 periodograms at grid points within the latitudinal band at 24°N considered in Figure 10e. Vertical dashed line indicates the local Coriolis frequency.

Appendix B: Mixed Layer Depth

The FLUX at MLB are derived from vertical velocity w and pressure p at the depth shown in Figure B1, which represent the deepest mixed layer depth (MLD) found in the FEB and SEP period. By definition, this depth should be deeper than the mean MLD. The overall spatial structures are comparable to those derived from the observations (de Boyer Montégut et al., 2004). Generally, the depths shown in Figure B1 are deeper than the observed ones in the mid- and high-latitude oceans, but comparable with the observed ones in the tropical and subtropical oceans. The deeper simulated MLD in the mid- and high-latitude oceans may result from larger variability of MLD there.
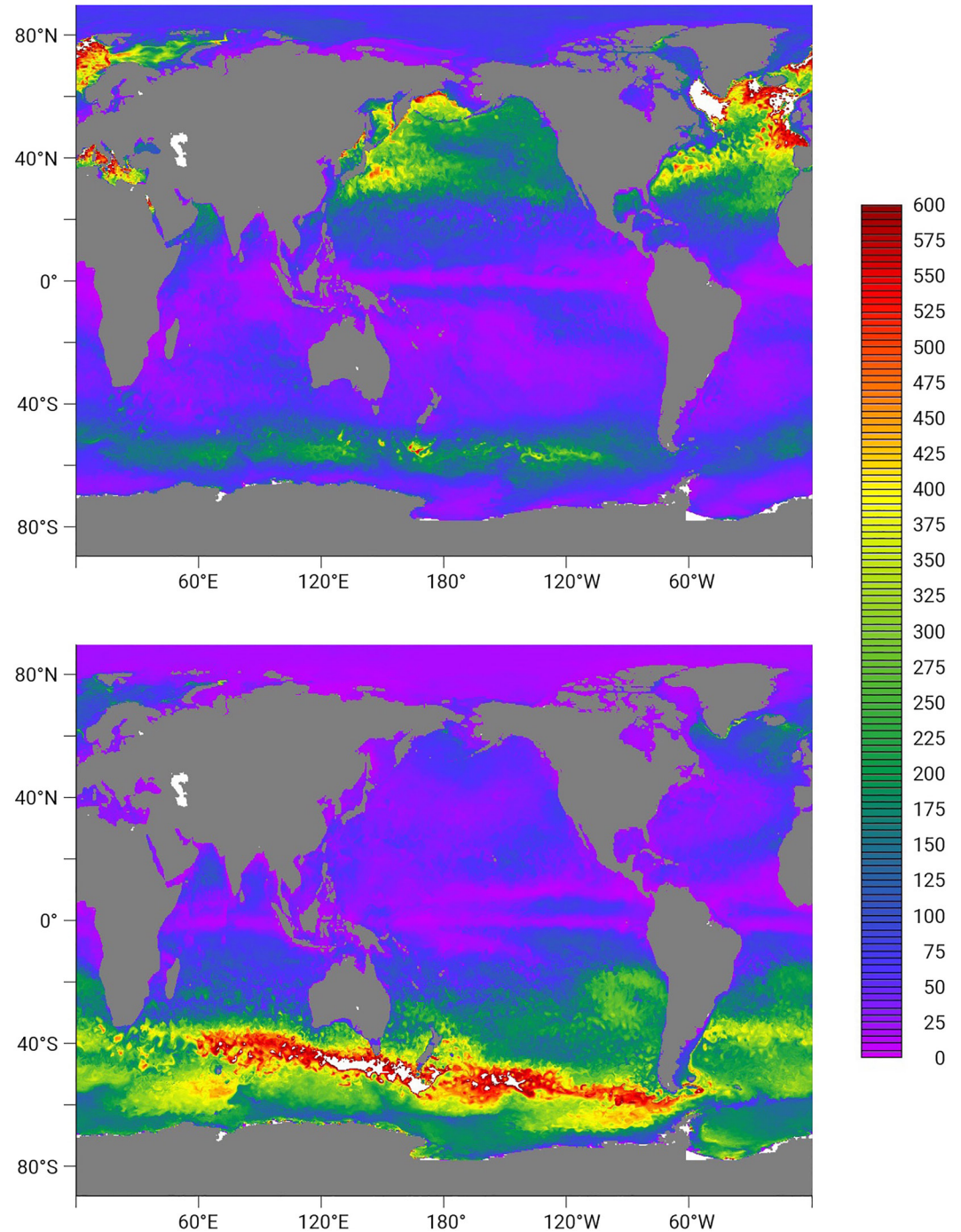
Figure B1. Deepest ocean mixed layer depth during the FEB (top) and the SEP (bottom) period simulated by the coupled ICON model, in meters.

Appendix C: Identifying the Contribution by Tropical Cyclones

The contribution of tropical cyclones to the surface INPUT and the MLB FLUX can be estimated in different ways. We choose to use a straight-forward way and visually select areas on the global map of the surface INPUT and MLD FLUX that are dominated by tropical cyclones activity. This map is then used to divide the surface INPUT and MLB FLUX into TC and non-TC contributions, which produces the numbers shown in Table 2. As

an example, Figure C1 shows the visually defined separation for estimating the TC and non-TC contributions to the surface INPUT.
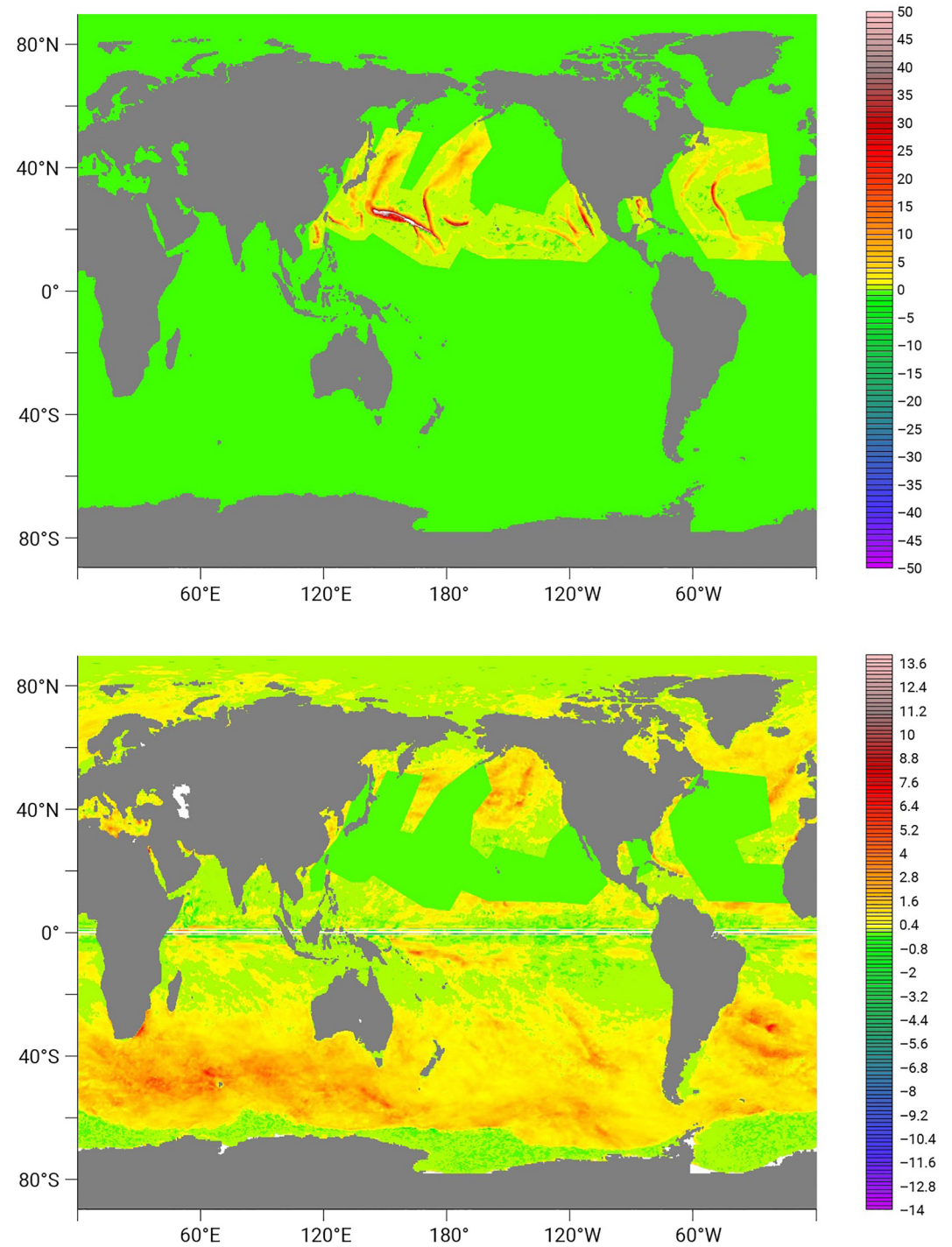

Figure C1. Separation of the surface INPUT due to contributions from tropical cyclones (top) and contributions without tropical cyclones (bottom). The uniform green color in the upper panel marks the area without, and the same uniform green color in the lower panel the area with contributions from tropical cyclones.

Data Availability Statement

A description of the simulation and the scripts used to produce the main results of this paper is archived in the publication repository of the Max Planck Society under http://hdl.handle.net/21.11116/0000-000A-C1FA-2.

References

Alford, M. H. (2001). Internal swell generation: The spatial distribution of energy flux from the wind to mixed layer near-inertial motions. *Journal of Physical Oceanography*, *31*(8), 2359–2368. https://doi.org/10.1175/1520-0485(2001)031<2359:isgtsd>2.0.co;2

Alford, M. H. (2003a). Improved global maps 54-year history of wind-work on ocean inertial motions. *Geophysical Research Letters*, *30*, 1–4. https://doi.org/10.1029/2002GL016614

Alford, M. H. (2003b). Redistribution of energy available for ocean mixing. *Nature*, *428*(6936), 159–162. https://doi.org/10.1038/nature01628

Alford, M. H. (2020). Global calculations of local and remote near-inertial-wave dissipation. *Journal of Physical Oceanography*, *50*(11), 3157–3164. https://doi.org/10.1175/JPO-D-20-0106.1. Retrieved from https://journals.ametsoc.org/view/journals/phoc/50/11/JPO-D-20-0106.1.xml

Alford, M. H., Mackinnon, J. A., Simmons, H. L., & Nash, J. D. (2016). Near-inertial internal gravity waves in the ocean. *Annual Review of Marine Science*, *8*(1), 95–123. https://doi.org/10.1146/annurev-marine-010814-015746

Baldauf, M., Seifert, A., Förstner, J., Majewski, D., Raschendorfer, M., & Reinhardt, T. (2011). Operational convective-scale numerical weather prediction with the COSMO model: Description and sensitivities. *Monthly Weather Review*, *139*(12), 3887–3905. https://doi.org/10.1175/mwr-d-10-05013.1

Boos, W. R., Scott, J. R., & Emanuel, K. A. (2004). Transient diapycnal mixing and the meridional overturning circulation. *Journal of Physical Oceanography*, *34*(1), 334–341. https://doi.org/10.1175/1520-0485(2004)034<0334:tdmatm>2.0.co;2

D'asaro, E. A. (1985). The energy flux from the wind to near-inertial motions in the surface mixed layer. *Journal of Physical Oceanography*, *15*(8), 1043–1059. https://doi.org/10.1175/1520-0485(1985)015<1043:tefftw>2.0.co;2

Dawe, J. T., & Thompson, L. (2006). Effect of ocean surface currents on wind stress, heat flux, and wind power input to the ocean. *Geophysical Research Letters*, *33*(6), L09604. https://doi.org/10.1029/2006GL025784

de Boyer Montégut, C., Madec, G., Fischer, A. S., Lazar, A., & Iudicone, D. (2004). Mixed layer depth over the global ocean: An examination of profile data and a profile-based climatology. *Journal of Geophysical Research*, *109*(C12), C12003. https://doi.org/10.1029/2004JC002378

Dipankar, A., Stevens, B., Heinze, R., Moseley, C., Zängl, G., Giorgetta, M., & Brdar, S. (2015). Large eddy simulation using the general circulation model ICON. *Journal of Advances in Modeling Earth Systems*, *7*(3), 963–986. https://doi.org/10.1002/2015ms000431

Eden, C., & Dietze, H. (2009). Effects of mesoscale eddy/wind interactions on biological new production and eddy kinetic energy. *Journal of Geophysical Research*, *114*(C5), C05023. https://doi.org/10.1029/2008JC005129

Eden, C., & Olbers, D. (2014). An energy compartment model for propagation, nonlinear interaction, and dissipation of internal gravity waves. *Journal of Physical Oceanography*, *44*(8), 2093–2106. https://doi.org/10.1175/jpo-d-13-0224.1

Emanuel, K. (2001). Contribution of tropical cyclones to meridional heat transport by the oceans. *Journal of Geophysical Research*, *106*(D14), 14771–14781. https://doi.org/10.1029/2000jd900641

Ferrari, R., & Wunsch, C. (2009). Ocean circulation kinetic energy: Reservoirs, sources, and sinks. *Annual Review of Fluid Mechanics*, *41*(1), 253–282. https://doi.org/10.1146/annurev.fluid.40.111406.102139

Firing, E., Lien, R.-C., & Müller, P. (1997). Observations of strong inertial oscillations after the passage of Tropical Cyclone Ofa. *Journal of Geophysical Research*, *102*(C2), 3317–3322. https://doi.org/10.1029/96jc03497

Flexas, M. M., Thompson, A. F., Torres, H. S., Klein, P., Farrar, J. T., Zhang, H., & Menemenlis, D. (2019). Global estimates of the energy transfer from the wind to the ocean, with emphasis on near-inertial oscillations. *Journal of Geophysical Research: Oceans*, *124*(8), 5723–5746. https://doi.org/10.1029/2018jc014453

Furuichi, N., Hibiya, T., & Niwa, Y. (2008). Model-predicted distribution of wind-induced internal wave energy in the world's oceans. *Journal of Geophysical Research*, *113*(C9), 1–13. https://doi.org/10.1029/2008jc004768

Gaspar, P., Grégoris, Y., & Levevfre, J.-M. (1990). A simple eddy kinetic energy model for simulations of the oceanic vertical mixing' tests at station papa and long-term upper ocean study site. *Journal of Geophysical Research*, *95*(C9), 16179–16193. https://doi.org/10.1029/jc095ic09p16179

Gill, A. (1984). On the behavior of internal waves in the wakes of storms. *Journal of Physical Oceanography*, *14*(7), 1129–1151. https://doi.org/10.1175/1520-0485(1984)014<1129:otboiw>2.0.co;2

Giorgetta, M. A., Brokopf, R., Crueger, T., Esch, M., Fiedler, S., Helmert, J., et al. (2018). ICON-A, the atmosphere component of the ICON Earth system model: I. Model description. *Journal of Advances in Modeling Earth Systems*, *10*(7), 1613–1637. https://doi.org/10.1029/2017MS001242

Gutjahr, O., Jungclaus, J. H., Brüggemann, N., Haak, H., & Marotzke, J. (2022). Air-sea interactions and water mass transformation during a katabatic storm in the Irminger Sea. *Journal of Geophysical Research: Oceans*, *127*(5). https://doi.org/10.1029/2021jc018075

Hersbach, H., Bell, B., Berrisford, P., Hirahara, S., Horányi, A., noz Sabater, M., et al. (2020). ICON-A, the atmosphere component of the ICON Earth system model: I. Model description. *Quarterly Journal of the Royal Meteorological Society*, *146*(730), 1999–2049. https://doi.org/10.1002/qj.3803

Hohenegger, C., Korn, P., Linardakis, L., Redler, R., Schnur, R., Adamidis, P., et al. (2022). ICON-sapphire: Simulating the components of the Earth System and their interactions at kilometer and subkilometer scales? Geoscientific Model Development Discussion. [preprint]. https://doi.org/10.5194/gmd-2022-171

Hohenegger, C., Korn, P., Linardakis, L., Redler, R., Schnur, R., Adamidis, P., et al. (2023). CON-Sapphire: Simulating the components of the Earth system and their interactions at kilometer and subkilometer scales. *Geoscientific Model Development*, *16*(2), 779–811. https://doi.org/10.5194/gmd-16-779-2023

Hohenegger, C., Kornblueh, L., Klocke, D., Becker, T., Cioni, G., Engels, J. F., et al. (2019). Climate statistics in global simulations of the atmosphere, from 80 to 2.5 km grid spacing. *Journal of the Meteorological Society of Japan*, *98*(1), 73–91. https://doi.org/10.2151/jmsj.2020-005

Jiang, J., Lu, Y., & Perrie, W. (2005). Estimating the energy flux from the wind to ocean inertial motions: The sensitivity to surface wind fields. *Geophysical Research Letters*, *32*(15), L15610. https://doi.org/10.1029/2005GL023289. Retrieved from https://agupubs.onlinelibrary.wiley.com/doi/abs/10.1029/2005GL023289

Jochum, M., Briegleb, B. P., Danabasoglu, G., Large, W. G., Norton, N. J., Jayne, S. R., et al. (2013). The impact of oceanic near-inertial waves on climate. *Journal of Climate*, *26*(9), 2833–2844. https://doi.org/10.1175/jcli-d-12-00181.1

Jungclaus, J., Lorenz, S. J., Schmidt, H., Brovkin, V., Brüggemann, N., Chegini, F., et al. (2021). The ICON Earth System model version 1.0. *Earth and Space Science Open Archive*. https://doi.org/10.1002/essoar.10507989.1

Klein, P. (2008). High-frequency winds and eddy resolving models. In M. W. Hecht, & H. Hasumi (Eds.), *Ocean modeling in an eddying regime* (pp. 83–100). American Geophysical Union. https://doi.org/10.1029/177GM07

Klein, P., Peyre, G., & Large, W. G. (2004). Wind ringing of the ocean in presence of mesoscale eddies. *Geophysical Research Letters*, *31*(15), L15306. https://doi.org/10.1029/2004GL020274

Korn, P. (2017). Formulation of an unstructured grid model for global ocean dynamics. *Journal of Computational Physics*, *339*, 525–552. https://doi.org/10.1016/j.jcp.2017.03.009

Korn, P., Brüggemann, N., Jungclaus, J., Lorenz, S., Gutjahr, O., Lorenz, S., et al. (2022). ICON-O: The ocean component of the ICON Earth System model – Global simulation characteristics and local telescoping capability. *Journal of Advances in Modeling Earth Systems*, *14*(10). https://doi.org/10.1029/2021ms002952

Kumar, A. U., Brüggemann, N., Smith, R. K., & Marotzke, J. (2021). Response of a tropical cyclone to a subsurface ocean eddy and the role of boundary layer dynamics. *Quarterly Journal of the Royal Meteorological Society*, *148*(742), 378–402. https://doi.org/10.1002/qj.4210

Liu, L. L., Wang, W., & Huang, R. X. (2008). The mechanical energy input to the ocean induced by tropical cyclones. *Journal of Physical Oceanography*, *38*(6), 1253–1266. https://doi.org/10.1175/2007jpo3786.1

Mauritsen, T., Redler, R., Esch, M., Stevens, B., Hohenegger, C., Klocke, D., et al. (2022). Early development and tuning of a global coupled cloud resolving model, and its fast response to increasing CO_2. *Tellus A: Dynamic Meteorology and Oceanography*, *74*(1), 346–363. https://doi.org/10.16993/tellusa.54

Munk, W., & Wunsch, C. (1998). Abyssal recipes II: Energetics of tidal and wind mixing. *Deep-Sea Research Part I*, *45*(12), 1977–2010. https://doi.org/10.1016/s0967-0637(98)00070-3

Niwa, Y., & Hibiya, T. (1997). Nonlinear processes of energy transfer from traveling hurricanes to the deep ocean circulation. *Journal of Physical Oceanography*, *102*, 464–471.

Olbers, D., & Eden, C. (2013). A global model for the diapycnal diffusivity induced by internal gravity waves. *Journal of Physical Oceanography*, *43*(8), 1759–1779. https://doi.org/10.1175/jpo-d-12-0207.1

Olbers, D., Jurgenowski, P., & Eden, C. (2020). A wind-driven model of the ocean surface layer with wave radiation physics. *Ocean Dynamics*, *70*(8), 1067–1088. https://doi.org/10.1007/s10236-020-01376-2

Pincus, R., Mlawer, E. J., & Delamere, J. S. (2019). Balancing accuracy, efficiency, and flexibility in radiation calculations for dynamical models. *Journal of Advances in Modeling Earth Systems*, *11*(10), 3074–3089. https://doi.org/10.1029/2019MS001621

Pincus, R., & Stevens, B. (2013). Paths to accuracy for radiation parameterizations in atmospheric models. *Journal of Advances in Modeling Earth Systems*, *5*(2), 225–233. https://doi.org/10.1002/jame.20027

Pollard, R. T., & Millard, R. C. (1970). Comparison between observed and simulated wind-generated inertial oscillations. *Deep-Sea Research and Oceanographic Abstracts*, *17*(4), 813–821. https://doi.org/10.1016/0011-7471(70)90043-4

Price, J. F. (1983). Internal wave wake of a moving storm. Part I. Scales, energy budget and observations. *Journal of Physical Oceanography*, *13*(6), 949–965. https://doi.org/10.1175/1520-0485(1983)013(0949:IWWOAM)2.0.CO;2. Retrieved from https://journals.ametsoc.org/view/journals/phoc/13/6/1520-0485_1983_013_0949_iwwoam_2_0_co_2.xml

Raddatz, T. J., Reick, C. H., Knorr, W., Kattge, J., Roeckner, E., Schnur, R., et al. (2007). Will the tropical land biosphere dominate the climate carbon cycle feedback during the twenty-first century? *Climate Dynamics*, *29*(6), 565–574. https://doi.org/10.1007/s00382-007-0247-8

Rai, S., Hecht, M., Maltrud, M., & Aluie, H. (2021). Scale of oceanic eddy killing by wind from global satellite observations. *Science Advances*, *7*(28), eabf4920. https://doi.org/10.1126/sciadv.abf4920. Retrieved from https://www.science.org/doi/abs/10.1126/sciadv.abf4920

Raja, K. J., Buijsman, M. C., Shriver, J. F., Arbic, B. K., & Siyanbola, O. (2022). Near-inertial wave energetics modulated by background flows in a global model simulation. *Journal of Physical Oceanography*, *52*(5), 823–840. https://doi.org/10.1175/JPO-D-21-0130.1. Retrieved from https://journals.ametsoc.org/view/journals/phoc/52/5/JPO-D-21-0130.1.xml

Rath, W., Greatbatch, R. J., & Zhai, X. (2013). Reduction of near-inertial energy through the dependence of wind stress on the ocean-surface velocity. *Journal of Geophysical Research: Oceans*, *118*(6), 2761–2773. https://doi.org/10.1002/jgrc.20198

Renault, L., Molemaker, M. J., McWilliams, J. C., Shchepetkin, A. F., Lemarié, F., Chelton, D., et al. (2016). Modulation of wind work by oceanic current interaction with the atmosphere. *Geophysical Physical Oceanography*, *46*(6), 1685–1704. https://doi.org/10.1175/JPO-D-15-0232.1

Rimac, A., von Storch, J. S., & Eden, C. (2016). The total energy flux leaving the ocean's mixed layer. *Journal of Physical Oceanography*, *46*(6), 1885–1900. https://doi.org/10.1175/jpo-d-15-0115.1

Rimac, A., Von Storch, J. S., Eden, C., & Haak, H. (2013). The influence of high-resolution wind stress field on the power input to near-inertial motions in the ocean. *Geophysical Research Letters*, *40*(18), 4882–4886. https://doi.org/10.1002/grl.50929

Sanford, T. B., Price, J. F., & Girton, J. B. (2011). Upper-ocean response to Hurricane Frances (2004) observed by profiling EM-APEX floats. *Journal of Physical Oceanography*, *41*(6), 1041–1056. https://doi.org/10.1175/2010JPO4313.1. Retrieved from https://journals.ametsoc.org/view/journals/phoc/41/6/2010jpo4313.1.xml

Stevens, B., Satoh, M., Auger, L., Biercamp, J., Bretherton, C. S., Chen, X., et al. (2019). The DYAMOND: The DYnamics of the Atmospheric general circulation Modeled On Non-hydrostatic Domains. *Progress in Earth and Planetary Science*, *6*(1), 61. https://doi.org/10.1186/s40645-019-0304-z

Watanabe, M., & Hibiya, T. (2002). Global estimates of the wind-induced energy flux to inertial motions in the surface mixed layer. *Geophysical Research Letters*, *29*(8), 2–5. https://doi.org/10.1029/2001gl014422

Wunsch, C., & Ferrari, R. (2004). Vertical mixing, energy, and the general circulation of the oceans. *Annual Review of Fluid Mechanics*, *36*(1), 281–314. https://doi.org/10.1146/annurev.fluid.36.050802.122121

Yang, B., & Hou, Y. (2014). Near-inertial waves in the wake of 2011 Typhoon Nesat in the northern South China Sea. *Acta Oceanologica Sinica*, *33*, 102–111. https://doi.org/10.1007/s13131-014-0559-6

Zängl, G., Reinert, D., Ripodas, P., & Baldauf, M. (2015). The ICON (ICOsahedral Non-hydrostatic) modelling framework of DWD and MPI-M: Description of the non-hydrostatic dynamical core. *Quarterly Journal of the Royal Meteorological Society*, *141*(687), 563–579. https://doi.org/10.1002/qj.2378

Zhai, X. (2017). Dependence of energy flux from the wind to surface inertial currents on the scale of atmospheric motions. *Journal of Physical Oceanography*, *47*(11), 2711–2719. https://doi.org/10.1175/jpo-d-17-0073.1